processes

MDPI

Article

Mechanistic Understanding of Field-Scale Geysers in Stormsewer Systems Using Three-Dimensional Numerical Modeling

Sumit R. Zanje [1,*], Pratik Mahyawansi [2], Abbas Sharifi [1], Arturo S. Leon [1], Victor Petrov [3] and Yuriy Yu Infimovskiy [4]

[1] Department of Civil and Environmental Engineering, Florida International University, Miami, FL 33174, USA
[2] Department of Mechanical and Materials Engineering, Florida International University, Miami, FL 33174, USA
[3] Department of Nuclear Engineering & Radiological Sciences, University of Michigan, 2355 Bonisteel Blvd., Ann Arbor, MI 48109, USA
[4] Department of Physics and Mathematics, Bauman Moscow State Technical University, Moscow 105005, Russia
* Correspondence: szanj001@fiu.edu

Abstract: Consecutive oscillatory eruptions of a mixture of gas and liquid in urban stormwater systems, commonly referred to as sewer geysers, are investigated using transient three-dimensional (3D) computational fluid dynamics (CFD) models. This study provides a detailed mechanistic understanding of geyser formation under partially filled dropshaft conditions, an area not previously explored in depth. The maximum geyser eruption velocities were observed to reach 14.58 m/s under fully filled initial conditions (h_w/h_d = 1) and reduced to 5.17 m/s and 3.02 m/s for partially filled conditions (h_w/h_d = 0.5 and 0.23, respectively). The pressure gradients along the horizontal pipe drove slug formation and correlated directly with the air ingress rates and dropshaft configurations. The influence of the dropshaft diameter was also assessed, showing a 116% increase in eruption velocity when the dropshaft to horizontal pipe diameter ratio (D_d/D_t) was reduced from 1.0 to 0.5. It was found that the strength of the geyser (as represented by the eruption velocity from the top of the dropshaft) increased with an increase in the initial water depth in the dropshaft and a reduction in the dropshaft diameter. Additionally, the Kelvin–Helmholtz instability criteria were satisfied during transitions from stratified to slug flow, and they were responsible for the jump and transition of the flow during the initial rise and fallback of the water in the dropshaft. The present study shows that, under an initially lower water depth in the dropshaft, immediate spillage is not guaranteed. However, the subsequent mixing of air from the horizontal pipe generated a less dense mixture, causing a change in pressure distribution along the tunnel, which drove the entire geyser mechanism. This study underscores the critical role of the initial conditions and geometric parameters in influencing geyser dynamics, offering practical guidelines for urban drainage infrastructure.

Keywords: computational fluid dynamics; combined sewer system; geyser eruption; sewer hydraulics; stormsewer geyser

check for updates

Academic Editors: Yuting Zhuo and Tianyu Wang

Received: 11 November 2024
Revised: 13 December 2024
Accepted: 17 December 2024
Published: 26 December 2024

Citation: Zanje, S.R.; Mahyawansi, P.; Sharifi, A.; Leon, A.S.; Petrov, V.; Infimovskiy, Y.Y. Mechanistic Understanding of Field-Scale Geysers in Stormsewer Systems Using Three-Dimensional Numerical Modeling. *Processes* **2025**, *13*, 32. https://doi.org/10.3390/pr13010032

1. Introduction

Urban deep tunnel drainage systems are mainly composed of the main near-horizontal tunnel and vertical dropshafts, the latter of which generally have a high hydraulic head and large discharge as well as aeration and air exhaust requirements [1,2]. Geysering is a common phenomenon observed in drainage systems during heavy rainstorms [3,4]. Geysers are high-frequency explosive ejections of a mixture of air–water from manholes in drainage systems [5,6]. Geyser occurrence is often related to air entrapment, its release from a pressurized flow, and flow transitions inside the tunnel. Although most storm or combined sewer systems are designed for gravity flow, a transition from gravity to surcharge flow can occur during high upstream influx and/or the submergence of their outlets [7]. Under unfavorable downstream conditions, air entrapment can occur due to a surcharge of flow. When entrapped air arrives at a ventilation structure such as a dropshaft, it may cause the high-frequency oscillatory release of the air–water mixture, which can attain a height of a few to tens of meters above ground level. A number of studies have focused on the physical process of geysering induced by air release through water-filled vertical shaft and pressure transients during such process [8–12]. Geysering is a rare occurrence; hence, there are few data regarding it [13].

Current studies on stormwater geysers mainly focus on the unsteady pressure dynamics and the air–water interactions in closed-conduit flow systems. For instance, Wright et al. (2011) [11] demonstrated the rapid ejection mechanisms in filled stormwater tunnels, while Leon et al. (2019) [5] provided rich information on the formation of oscillatory eruptions. Despite these advances, the influences of the dropshaft geometries and unsteady flow characteristics in real-world applications have not been explored adequately. These are important to address in order to mitigate geysers, which are a serious risk to infrastructure integrity and public safety in densely populated urban areas. Understanding geyser behavior helps to prevent them from occurring and informs the optimization of ventilation systems in stormwater networks. This research provides the scientific community with validated numerical tools for the simulation of complex two-phase flows, hence creating a foundation for further studies on transient hydraulics and infrastructure resilience. Moreover, insight into the transitions of flow and instability mechanisms gives actionable guidelines for the implementation of flow stabilization techniques, such as pressure relief chambers or enhanced ventilation designs. Such a two-way approach—an initial mechanistic understanding, followed by practical application—addresses both the theoretical and operational challenges of geyser mitigation, advancing the state of the art in stormwater management.

The findings from this study, although based on simplified configurations, provide transferable insights into the mechanisms of geyser formation, including pressure gradients, air pocket entrainment, and air–water interactions, which are applicable across systems of varying scales and geometries. Our earlier work on small-scale experimental setups (Mahyawansi et al., 2024 [14]) demonstrated critical flow structures such as slug formation, eruption dynamics, and oscillatory pressure behavior under controlled laboratory conditions. However, small-scale studies are inherently limited in their ability to capture field-specific complexities, including irregular geometries, multi-phase flow instabilities, and non-uniform inflows. To address these limitations, the large-scale numerical simulations presented in this study incorporate parametric variations in dropshaft dimensions and initial and boundary conditions to better replicate the complexities of real-world stormwater and sewer systems. The validated numerical framework presented in this study, with experimental work presented in Mahyawansi et al. (2024) [15], provides a robust foundation for the scaling and extension of the results to stormwater and combined sewer systems with more intricate layouts.

There are two major differences between the current study and the previous studies reported by Leon, A. S. (2019) [5]: (1) the dropshaft is in a partially filled condition; (2) a continuous flow of air and water is provided in the system. This study is organized as follows. First, the numerical methodology, including the governing equations and initial and boundary conditions, is briefly described. Second, the mechanism that leads to the violent geyser in the stormsewer and combined sewer system is elucidated based on a numerical model. Third, the numerical models are used to study the effect of the initial water level in the dropshaft and the dropshaft diameter on the formation of the geyser using four CFD cases that capture a range of key physical conditions commonly encountered in stormwater systems. These specific cases were selected to highlight critical mechanisms contributing to geyser formation and intensity. By focusing on these unique scenarios, this study provides a detailed mechanistic understanding of the phenomena, which is essential for the development of effective mitigation strategies. Finally, the key results are summarized.

2. Methodology

2.1. Numerical Model Description

Figure 1 outlines the stepwise process used in this study to investigate the mechanistic behavior of geysers in stormwater systems. This workflow incorporates the numerical modeling setup, calibration, parametric simulations, and result interpretation to ensure a robust and comprehensive analysis.

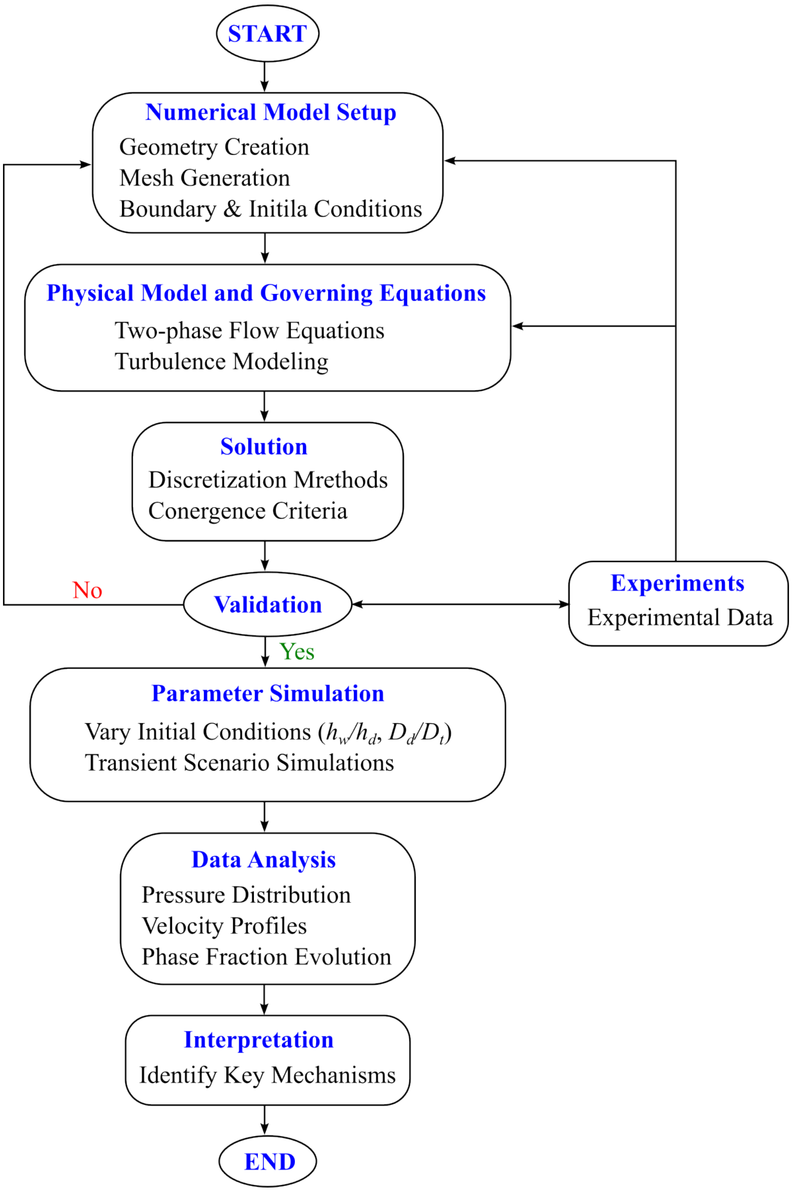

Figure 1. Workflow for the mechanistic study of geysers in stormwater systems using CFD.

The numerical methods used in this work rely on a cell-centered, co-located finite volume method (FVM), which is implemented using the open-source CFD software OpenFOAM V6. The present finite volume code is based on the pressure-based two-phase solver compressibleInterFoam. compressibleInterFoam is a solver for two compressible, immiscible, non-isothermal phases (liquids and/or gases), whereby the interface is captured by the volume of fluid approach [16]. Details on the numerical approach of OpenFOAM can be found in Jasak, H. (1996) [17]. This solver uses three-dimensional (3D) equations for two phases, i.e., air and water, using the volume of fluid (VOF) method, with special emphasis on maintaining a sharp free surface (interface-capturing solver) [18]. The water phase is treated as a perfect compressible fluid, $\rho_w = \rho_{w,0} + p/R_w T$ with $\rho_{w,0} = 998.9$ kg/m^3 and $R_w = 3000$ J/kgK [19], while the air phase is a compressible perfect gas, $\rho_a = p/R_a T$ with $R_a = 287$ J/kgK [20]. This method uses the volume fraction indicator function α to determine the amount of liquid present in each cell. In this study, $\alpha = 1$ and $\alpha = 0$, and the cell volume is considered filled with water and air, respectively. The cell contains the free surface for $1 > \alpha > 0$ as it is partially filled. Based on the assumption of a homogeneous mixture, the cell-specific density (ρ) and viscosity (μ) are calculated by

$$\rho = \alpha\rho_w + (1-\alpha)\rho_a \ , \tag{1}$$

$$\mu = \alpha\mu_w + (1-\alpha)\mu_a \ . \tag{2}$$

Based on Equation (1), the total mass continuity equation can be written as

$$\frac{\partial\rho}{\partial t} + \nabla\cdot\rho\boldsymbol{U} = 0 \ . \tag{3}$$

To track the interface of the two compressible phases, the water volume fraction transport equation is presented in Equation (4), which is solved explicitly with the MULES schemes in several sub-cycles within a time step [21]:

$$\frac{\partial\alpha}{\partial t} + \nabla\cdot(\boldsymbol{U}\alpha) + \nabla\cdot\boldsymbol{U}_{\mathbf{c}}\alpha(1-\alpha) = \alpha(1-\alpha)\left(\frac{\psi_a}{p_a} - \frac{\psi_w}{p_w}\right)\cdot\frac{Dp}{Dt} + \alpha\nabla\cdot\boldsymbol{U} \ . \tag{4}$$

The third term used in the L.H.S. of Equation (4) is used to sharpen the interface and avoid numerical diffusion [22]. $\boldsymbol{U}_{\mathbf{c}}$ denotes the relative velocity of the two fluids, which is taken to be normal to the air–water interface. $\boldsymbol{U}_{\mathbf{c}}$ is computed at the cell face center of a computational cell, as shown in Equation (5).

$$\boldsymbol{U}_{\mathbf{c,f}} = c_\alpha\frac{|\phi_f|}{|S_f|}\boldsymbol{n}_f \ , \tag{5}$$

where c_α (less than 1) is a parameter that is used to adjust the strength of the compression of the interface, ϕ_f is the volume flux through the face, S_f is the surface area vector, and $\boldsymbol{n}$ represents the unit normal to the interface surface determined by $\boldsymbol{n} = \nabla\alpha/|\nabla\alpha|$. The R.H.S. of Equation (4) takes into account the pressure (p) and influence of specific compressibility (ψ) of both of the phases.

The single momentum equation for the homogeneous mixture is given by Equation (6).

$$\frac{\partial\rho\boldsymbol{U}}{\partial t} + \nabla\cdot(\rho\boldsymbol{U}\boldsymbol{U}) - \nabla\cdot(\mu_{eff}\nabla\boldsymbol{U}) = \sigma\kappa\nabla\alpha - \boldsymbol{g}\cdot\boldsymbol{x}\nabla\rho - \nabla p_d \ , \tag{6}$$

where ρ is the density of the mixture (Equation (1)), σ is the surface tension [23], and $\kappa = -\nabla \cdot (\nabla\alpha/|\alpha|)$ is the curvature of the interface, $g = 9.81$ m/s^2 is the gravity vector, x is the position vector, and $p_d = p - \rho \boldsymbol{g} \cdot \boldsymbol{x}$ is the piezometric pressure [24].

Finally, an additional transport equation for the temperature T is deducted from the energy equation as stated in Equation (7):

$$\frac{\partial \rho T}{\partial t} + \nabla \cdot (\rho \boldsymbol{U} T) - \triangle(\mu_{eff} T) = -\left(\frac{\alpha}{c_{v,w}} + \frac{1-\alpha}{c_{v,a}}\right)\left(\frac{\partial \rho k}{\partial t} + \nabla \cdot (\rho \boldsymbol{U} k) + \nabla \cdot (\boldsymbol{U} p)\right), \quad (7)$$

with $c_{v,w} = 4182$ J/kgK and $c_{v,a} = 1007$ J/kgK as the specific heat capacities at a constant volume for water and air, respectively, and $k = |U|^2/2$.

To model the turbulence phenomenon considering the RANS approach, a realizable $k - \varepsilon$ turbulent model was used. The suitability of the realizable $k - \varepsilon$ turbulent model in simulating geyser events is already presented in previous studies [25,26]. This turbulence model uses two closure equations for k (turbulent kinetic energy) and ε (energy dissipation). The realizable $k - \varepsilon$ model used in this study is based on Shih et al., (1995) [27].

The fluid properties used in this study are listed in Table 1.

Table 1. Fluid properties used in numerical simulation (adapted from Mahyawansi et al. (2024) [15]).

Parameter	Water	Air
Density (kg/m^3)	998.4	1.22
Dynamic viscosity (Pa·s)	1.003×10^{-3}	1.789×10^{-5}
Surface tension	0.072	

2.2. Computational Geometry and Mesh

A schematic of this experimental setup is shown in Figure 2, and Table 2 presents the geometrical parameters of the setup. The model consisted of the following parts: (1) a total upstream horizontal pipe ($Lu_1 + Lu_2$) of 40 m in length and 0.152 m in diameter, (2) a horizontal downstream pipe (Ld) of 6 m in length and 0.152 m in diameter, (3) a constant air supply into the upstream horizontal pipe at a distance of 30 m from the extreme upstream end, (4) a 6.096 m long dropshaft with a diameter of 0.152 m and at a distance of 40 m from the extreme upstream end, and (5) an atmospheric domain above the dropshaft that is modeled as a cylinder with a diameter of 1 m and a height of 6 m. Table 3 provides a summary of the simulated runs in this study.

The computational domain was discretized using OpenFOAM meshing utilities such as blockMesh and snappyHexMesh. First, a hexahedral base mesh was created using blockMesh; later, snappyHexMesh was used to adapt the mesh to the surface of the CAD geometry by iteratively refining and morphing the base mesh. A snapshot of the generated 3D mesh is presented in Figure 2c,d. The generated three-dimensional (3D) mesh was a hybrid consisting of hexahedra (hex) and split-hexahedra (split-hex) elements [28]. The hybrid mesh was selected due to its suitability to match appropriate cells with the boundary surface and allocate different cells of various element types in other parts of the complex flow regions (such as at the junction where the horizontal sections connect the vertical sections). It leads to an accurate solution and better convergence than using only either a structured or unstructured mesh [29]. In this study, the numerical model is discretized using 1,422,275 boundary-fitted cells. The tunnel and dropshaft's cross-section is discretized using 22 cells along the diameter, with a finer mesh closer to the wall. The maximum cell size of 0.01 m is used for the discretization, which is suggested by Chegini, T. and Leon, A. S. (2019) [25], to accurately simulate the geyser eruption based on a mesh convergence study.

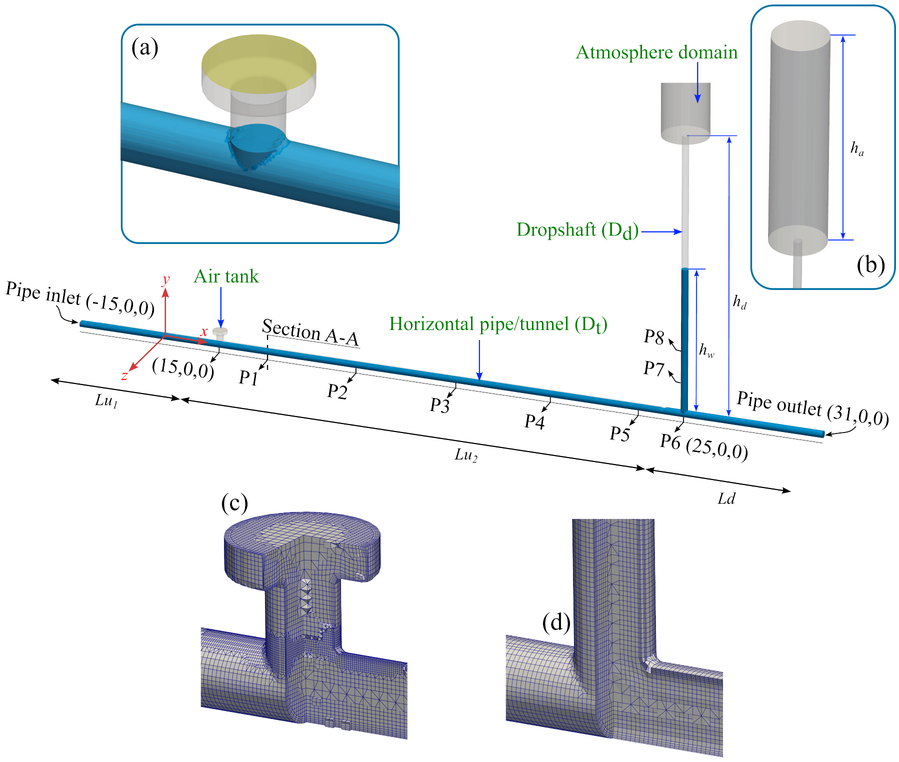

Figure 2. Schematic of the geyser computational setup and boundary conditions of the numerical model. The system includes an upstream horizontal pipe (40 m in length, 0.152 m diameter), a downstream horizontal pipe (6 m in length, 0.152 m diameter), and a vertical dropshaft (6.096 m height, 0.152 m diameter). Subfigures illustrates: (**a**) a close-up view of the interface between the air and water domains in the horizontal pipe at air tank, (**b**) the vertical dropshaft and the atmospheric domain, (**c**) computational mesh for the horizontal pipe-air tank junction, (**d**) computational mesh for the horizontal pipe-dropshaft junction.

Table 2. Geometry parameters of the numerical setup.

Parameters	Value (m)	Description
D_t	0.152	Diameter of horizontal pipe/tunnel
D_d	0.152	Diameter of dropshaft
Lu_1	30.0	Length of upstream pipe from extreme upstream end to air tank
Lu_2	10.0	Length of upstream pipe from air tank to dropshaft
Ld	6.0	Length of downstream pipe
h_d	6.096	Height of dropshaft
h_a	6.0	Height of atmosphere domain
h_w	1.42	Initial water level in dropshaft

Table 3. Summary of simulation runs.

Case	h_w/h_d	D_d/D_t
Case 1	0.23	1.0
Case 2	0.5	1.0
Case 3	1.0	1.0
Case 4	0.5	0.5

The mesh size was chosen based on the mesh independence test (Figure 3). The test indicator was the transient pressure at P6 during case 2 (i.e., h_w/h_d = 0.5). A series of gradually refined mesh levels were used for the CFD simulation. The mesh levels were approximately 360,591 for the coarse mesh, 1,422,275 for the medium mesh, and 3,074,009 for the fine mesh. It was found that the results for the medium mesh and fine mesh were similar. Since the computational time from the fine mesh to medium was significantly lower and there were negligible differences in performance between the two mesh levels, a medium mesh was used for the remaining simulations. The numerical results were compared with the experimental data, which showed that the model captured the significant characteristics associated with the experimental data, with some discrepancies. The detailed experimental setup and results are presented in Mahyawansi et al. (2024) [15]. The observed discrepancies between the experiment and the numerical results aptly illustrate the complexity of two-phase flows and the associated flow behavior at the field scale. Given that all efforts to reproduce actual field-scale conditions were applied in the experiments and simulations, it was expected that small differences would arise. First, it is important to note that the complexity of fluids in two-phase flows in field-scale setups naturally leads to differences in the experimental and numerical results. Second, it is worth highlighting the meticulousness of this experimental setup, which included components like elbows, joints, and valves. Every effort was made to ensure the fidelity of the experimental apparatus to field-scale conditions. However, it is crucial to recognize that the presence of such components may introduce subtle flow perturbations or variations not fully captured in numerical simulations. These localized effects could be the source of the observed differences between the experimental and numerical results.

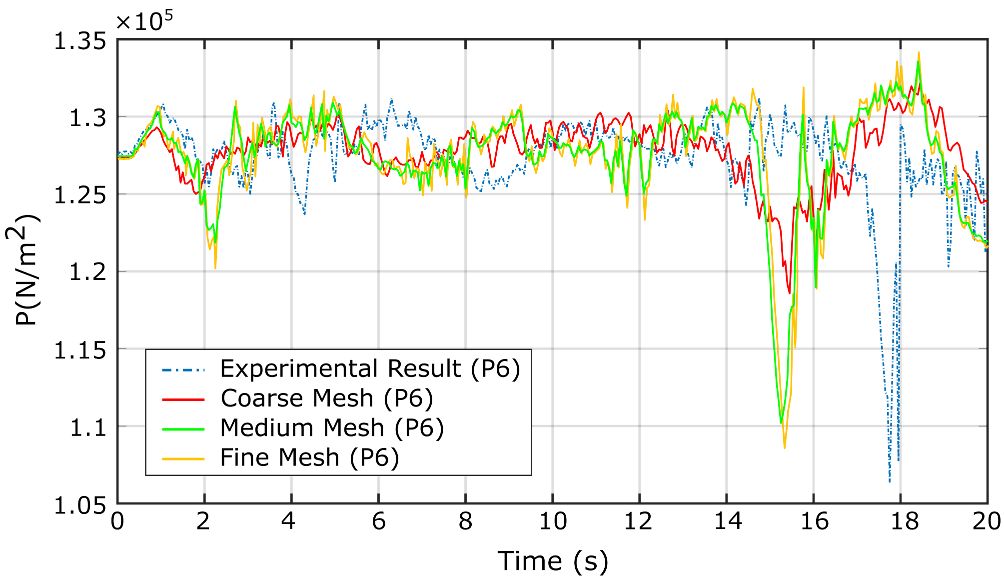

Figure 3. Comparison of experimental results with simulations for the mesh convergence study at pressure probe P6.

2.3. Definition of Initial Control Parameters and Boundary Conditions

Five boundary patches were prescribed for the numerical model (Figure 2): *inlet*, *outlet*, *tank*, *pipe wall*, and *atmosphere*. For the realizable $k-\varepsilon$ turbulence model, OpenFOAM requires six types of boundary conditions (BC) for each boundary. They are *alpha.water* (water phase fraction in cell volume), *p_rgh* (transformed pressure relative to datum, $\mathrm{N/m^2}$), U (velocity vector, m/s), T (temperature, K), k (turbulent kinetic energy, $\mathrm{m^2/s^2}$), and ε (energy dissipation, $\mathrm{m^2/s^3}$). The first three BCs are required for hydraulic modeling, while the last three are required for turbulence calculation. For *inlet* and *outlet*, pressure data were prescribed to achieve the pressure-driven flow. The *inlet* was applied with *prghTotalPressure* and the *outlet* with *prghPressure*. The velocity (U) BCs for *inlet* and *outlet* were *pressureInletOutletVelocity* and *inletOutlet*, respectively. The atmospheric domain was kept as *pressureInletOutletVelocity* with velocity and pressure as *totalPressure*, so that air could be exchanged if necessary. The boundary conditions for the tank were kept as *pressureIn-*

letOutletVelocity velocity and *totalPressure* pressure. All the wall BCs were kept in a no-slip condition (i.e., velocity = 0). The initial temperature of the water and air in the system was 26.85 °C. The atmospheric pressure was set to 102,032 Pa. For the turbulent approach, values of k and ε were calculated [30,31]. The applicability of the turbulence model in capturing similar geyser phenomena has been established in previous studies, such as those by Chegini and Leon (2019) [25], Chegini and Leon (2018) [32], and Qian et al. (2020) [6], where it successfully resolved transient air–water interactions and pressure fluctuations in stormwater and sewer systems. All *walls* are specified as *wallFunctions*, reducing the necessity of fine-layered boundary layers and hence the computational time. For the automatic time step adjustment, *adjustableRunTime* was used with minimum $\triangle t = 10^{-8}$, keeping the maximum Courant–Friedrichs–Lewy/Courant number (CFL=$\overrightarrow{u}\triangle t/\triangle x$) to 0.5. To ensure the stability of a model and improve its accuracy, the maximum value of the Courant number should be less than 1 [33]. The simulation was run on 32 processors using the distributed parallel *decomposePar* computing utility (AMD Ryzen Threadripper 3960X 3.8 GHz 32-Core sTRX4 Processor).

The merged PISO-SIMPLE (PIMPLE) scheme is used to couple the pressure and velocity. The PIMPLE algorithm is the coupling model between PISO (Pressure Implicit with Splitting of Operators) and SIMPLE (Semi Implicit Method for Pressure Linked Equations) to solve the RANS equations [34]. A detailed description of the PISO and SIMPLE algorithms can be found in [35,36]. This study uses a transient scheme called Euler for temporal discretization. OpenFOAM also provides other high-resolution transient discretization schemes, such as CrankNicolson and backward, which are second-order accurate but are unbounded [19]. The unbounded behavior of these schemes may result in a non-feasible solution to the problem [37]. The Euler scheme is a first-order bounded implicit scheme, which is sufficiently accurate due to the small time steps created by the Courant number restriction; hence, it is the best option for this case. This study uses the default Gauss linear scheme for gradient discretization and a second-order scheme with a flux limiter scheme for divergence discretization [38]. Convergence is declared when the normalized residual is less than 10^{-6} for pressure (*p_rgh*) and 10^{-8} for all other variables (*alpha.water*, k, ε, U, and T).

The simulation is performed in two stages. First, the steady-state flow is achieved in the horizontal pipe without supplying air. This stage is necessary to ensure that the flow is fully developed and help to decide the position of the air tank (i.e., to ensure initial smooth advancement, the air tank should be connected beyond the hydrodynamic entrance region). Once the steady state is confirmed (using the velocity profile along the length of the horizontal pipe at multiple cross-sections), the input fields are mapped to the second mesh (i.e., having the air tank connected to the tank) using the *mapFields* utility. As suggested by Leon, Elayeb, and Tang (2019) [39], the tank pressure was set to a specific value, ensuring that, immediately before air entered the horizontal pipe, the water and air were quiescent and in an apparent equilibrium.

3. Mechanisms That Lead to Geysering in Stormwater

The mechanism is described using one of the partially filled conditions (Case 1) in which the initial water level in (h_w) is 1.42 m, and both the tunnel and dropshaft diameters (D_t and D_d) are 0.152 m. The simulation results are analyzed using (1) the velocity of the air and water phases inside the horizontal pipe, (2) pressure probe data along the horizontal pipe and dropshaft, and (3) phase fraction data inside the horizontal pipe and dropshaft.

The numerical observations are summarized in schematics (Figures 4 and 5). The geyser produced in the numerical simulations consisted of several violent eruptions, which lasted a few seconds. This setup differs from the experimental work of Leon, Elayeb, and

Tang (2019) [39], where the continuous flow of the water in the tunnel was not simulated. It is worth mentioning that the violent eruptions produced resembled the characteristics of those that occur in actual stormwater and combined sewer systems.

The main mechanism that leads to geysering in the partially filled dropshaft system can be summarized as follows.

(1) The horizontal pipe transports the enormous air pocket that forms during the rapid filling of near-horizontal tunnels towards the dropshaft without causing noticeably significant fluctuations, as shown in Figures 4a and 6a,b [5,39]. This can be corroborated by Figure 10a for a time less than about t = 12.20 s when the air pocket front arrives at the base of the dropshaft. It is noted that, before about 12.20 s, the air pocket in the horizontal pipe advances very slowly, as there is no significant initial pressure gradient. Thus, before about 12.20 s, the flow regime in the horizontal pipe is stratified. Figure 10 shows transient pressure variations at all data points, replicating the oscillatory patterns observed in Mahyawansi et al. (2024) [15].

Figure 11 shows the pressure distribution curves of the central axis of the horizontal pipe from x = 16 m to 25 m at certain moments (during the initial smooth advancement of trapped air towards the dropshaft, t = 1 s to 12.3 s). The data show that the pressure gradually decreases from upstream to downstream of the horizontal pipe at the beginning (t = 1 s). As the air pocket starts advancing, a small sharp rise appears at the tip of the advancing air pocket. At t = 12.3 s, the figure shows relatively lower but gradual variation from upstream to downstream. This is because a clear passage for the air pocket has been created, and the air pocket front reaches the base of the dropshaft. The water level in the dropshaft is almost the same during this time interval (Figure 8a,b).

(2) At t = 12.3 s, the initial air pocket reaches the bottom of the dropshaft (Figures 6c and 8c). This large air pocket enters the dropshaft and rises in the form of a Taylor-like bubble due to buoyancy. Like a classical Taylor bubble, the free surface of the water in the dropshaft is lifted upward with the ascending air pocket until it breaks the free surface. This can be observed in Figure 8d–h. When the air penetrates the dropshaft, the hydrostatic head of the dropshaft decreases till it reaches 110,262 N/m^2 at t = 13.58 s (Figure 10b). This sudden drop in hydrostatic pressure in the dropshaft creates a significant pressure gradient along the horizontal pipe.

Figure 12 shows the variation in the differential pressures ($\triangle P$) measured during time interval t = 11.5 s to 14 s. The $\triangle P_{16\_25}$ represents the pressure difference between points $P1$ and $P6$. As speculated, no significant variations in the differential pressures were observed till t = 12.3 s due to the smooth advancement of the air towards the dropshaft. As the air enters the dropshaft, it builds the differential pressure along the horizontal pipe, causing an increase in the pressure gradient and hence accelerating the air and water in the horizontal pipe. This can be seen in Figure 13 at approximately t = 12.35 s to t = 13.35 s. It is worth mentioning that, inside the horizontal pipe during this process, the air velocity leads to water velocity, which is due to the significant difference in the inertia of the two phases [40]. The relative rise in the air and water velocity results in Kelvin–Helmholtz (KH) instability. These results align with the observations reported by Leon, Elayeb, and Tang (2019) [39], who speculated that KH instability might be responsible for the flow regime transition based on experimental snapshots. While their study estimated air velocities exceeding 5 m/s from experimental frames, the absence of direct air velocity measurements left this hypothesis partially unverified. As shown in Figure 13, the numerical results reveal the growth of interfacial waves due to velocity shear between the air and water phases, a hallmark of KH instability. These waves grow rapidly, leading to flow breakdown and the onset of slug flow, consistent with the mechanism hypothesized by Leon (2019) [5].

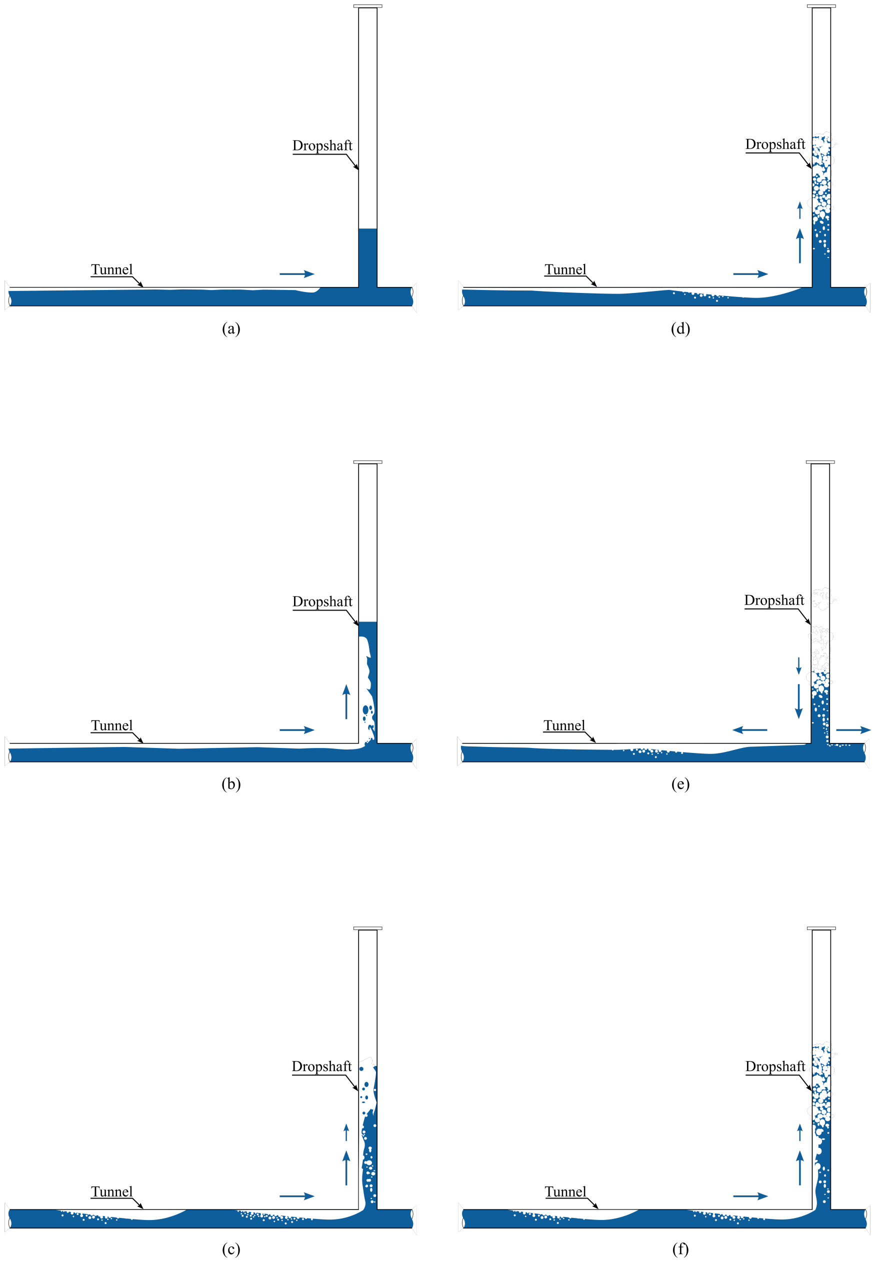

Figure 4. Geyser processes: (**a**) air pocket approaching dropshaft, (**b**) rising of Taylor-like bubble in dropshaft, (**c**) first air pocket release and formation of liquid slugs, (**d**) first temporary blockage created at junction, (**e**) first fallback of water inside dropshaft, (**f**) formation of new slugs due to successive mixing.

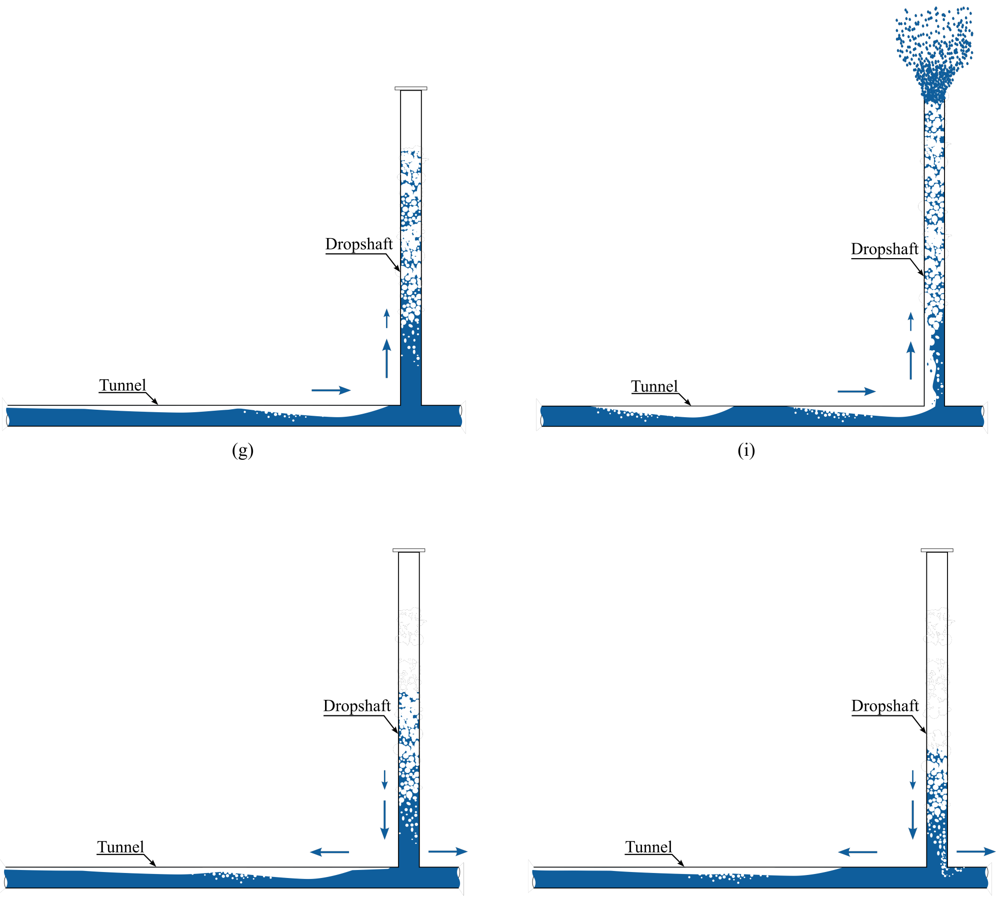

Figure 5. Geyser processes: (**g**) second temporary blockage created at the junction, (**h**) second fallback of water inside dropshaft, (**i**) eruption due to blowout of the slug, (**j**) fallback of water inside dropshaft after the first erruption.

To further analyze the stability of the wave (air water interface), Taitel and Dukler (1976) [41] suggested KH instability to occur when the low pressure at the crest overcomes the stabilizing effect of gravity. The condition for wave growth is as shown in Equation (8) (Figure 15):

$$P - P' > (h_G - h'_G)(\rho_L - \rho_G)g \ , \tag{8}$$

with

$$P - P' = \frac{1}{2}\rho_G({U'_G}^2 - {U_G}^2) \ , \tag{9}$$

where P and P' are the pressure for stratified and interfacial wave conditions, respectively. U_G and U'_G are the gas (i.e., air) velocities for stratified and interfacial wave conditions, respectively. h_G and h'_G are the gas depths above stratified and interfacial wave conditions, respectively. ρ_G is the gas (i.e., air) density, ρ_L is the liquid (i.e., water) density, and g is the gravitational acceleration. Using Equations (8) and (9), the criteria for instability become

$$U_G > C_1 \left[\frac{g(\rho_L - \rho_G)h_G}{\rho_G}\right]^{\frac{1}{2}} \ , \tag{10}$$

in which

$$C_1 = \left[\frac{2}{\frac{h_G}{h'_G}\left(\frac{h_G}{h'_G} + 1\right)} \right]^{\frac{1}{2}}, \tag{11}$$

where parameter C_1 reflects the size of the interfacial wave. Taitel and Dukler (1976) [41] further mentioned that C_1 also could be determined from Equation (12):

$$C_1 = 1 - \frac{h_L}{D}, \tag{12}$$

Hence, Equation (10) can be expressed as Equation (13):

$$U_G > \left[1 - \frac{h_L}{D}\right] \left[\frac{g(\rho_L - \rho_G)h_G}{\rho_G}\right]^{\frac{1}{2}}. \tag{13}$$

It can be seen from Figure 6e that a series of interface waves are formed inside the horizontal pipe under the gas as the velocity rises, creating a vertical pressure gradient along the diameter. The interface becomes unstable due to the momentum transfer between the air and water. The wave tends to increase as the gas accelerates because of the Bernoulli effect, which causes the pressure in the gas phase over the wave to decrease. The interface wave is increased when the pressure differential between the phases overcomes the interfacial tension and gravity [42–44].

To validate this, the aerodynamic pressure gradient and velocity variation over a wave at two distinct instances (t = 12.1 s and 13.55 s) are plotted in Figure 16. It shows one at stratified flow and another at transition flow conditions, when instabilities began to occur as the aerodynamic lift on the wave was sufficient to overcome the hydrostatic forces. The figure shows the smooth variation in the pressure and velocity over the wave along the pipe (near the crown of the horizontal pipe) under stratified conditions (t = 12.1 s). As air penetrated into the dropshaft, it increased the pressure gradient along the horizontal pipe and increased the velocities of the air and water. Air flows at a high velocity above the wave crest, and a vertical pressure gradient is created owing to the Bernoulli effect [45]. The momentum transfer between air and water causes the initiation of small perturbations over the interface. At t = 13.55 s, Figure 16 (Domain 1 and Domain 2) shows the pressure drop above the interface where the water surface starts elevating. The Bernoulli effect leads to an increase in velocity in this region, causing a further increase in the wave, which leads to the transition from stratified to wavy and ultimately to slug flow (Figure 6e–h). As per Sanchis, Johnson, and Jensen (2011) [46], the flow field inside the horizontal pipe during the transition is dominated by large-amplitude waves.

To further support this theory, the instability criteria mentioned in Equation (13) are plotted as shown in Figure 17 [41]. As shown in the figure, the velocity of gas (U_G) in the horizontal pipe starts increasing as air starts ingesting into the dropshaft, and, at t = 13.05 s, it overcomes the R.H.S. term of Equation (13). This satisfies the instability criteria to cause the transition from stratified to slug flow. It is worth mentioning that the KH instability provides a mechanism for the initiation of jumps and transitions; however, after the initial rise and fallback of the water, the validity of the instability criteria in the subsequent cycles is not guaranteed.

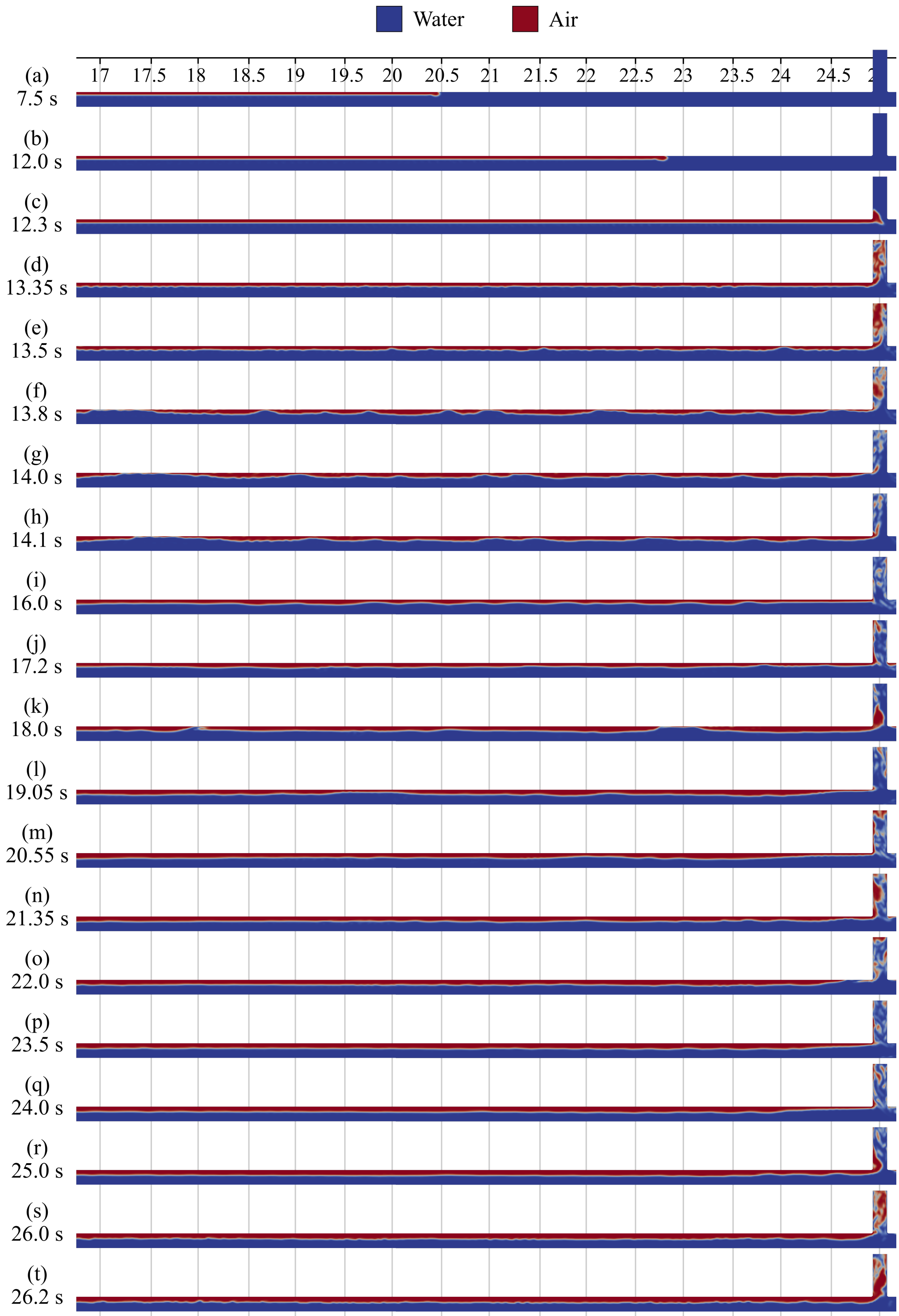

Figure 6. Snapshots of air–water phase fraction in the horizontal pipe (Case 1).

When the first slug passed the intersection, some liquid was siphoned into the dropshaft due to lower pressure, causing a partial or complete blockage to the supply of air from the horizontal pipe (Figures 4d and 6f,g) [47]. This stage is referred to as 'the blockage of the dropshaft base'. As a consequence, the pressure at the bottom of the dropshaft increases, pushing the air–water interface in the horizontal pipe further away from the dropshaft base and compressing the accumulated gas in the horizontal pipe (Figure 10b). On the way up, air rises further into the dropshaft, followed by a trailing mixture of air and water (like a churning flow), called a slug jump. The ascending air inside the dropshaft causes the liquid film to rise to a certain height. However, the shear force acting on the film is not enough to balance the gravitational force due to the scarcity of the air supply from the horizontal pipe. As a result, the film decelerates its upward velocity slowly and then accelerates to fall towards the junction. The flowing water through the horizontal pipe further carries the falling film towards the downstream end. It should be noted that the ascending air could not produce the initial spillage due to the quite low initial water level in the dropshaft (i.e., $h_w/h_d = 0.23$). The pressure at the dropshaft base decreases during this fallback stage (Figure 10b at t = 14.4 s to 17.2 s). This can be corroborated by Figure 14, as the water volume fraction inside the dropshaft decreases during this stage. The corresponding air–water phase fraction during this stage can be seen in Figure 8i,j. The increase and decrease in the water volume fraction inside the dropshaft during the initial blockage and fallback stage are referred to as cycle 1 in Figure 14.

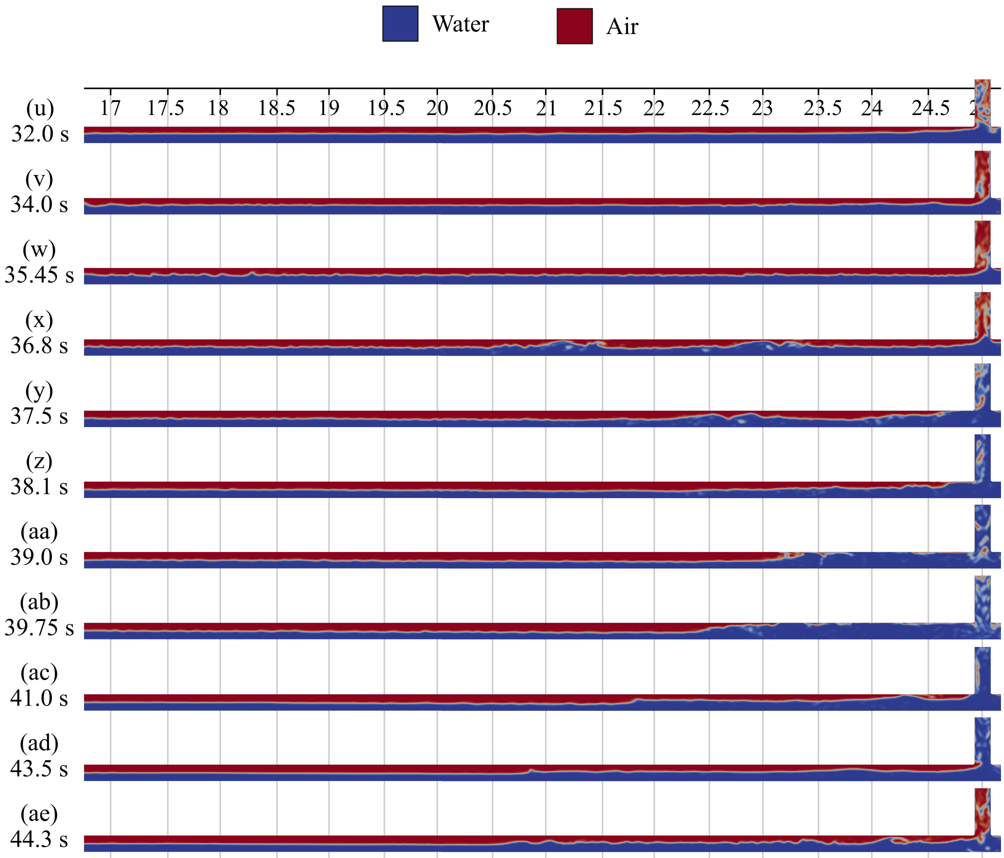

Figure 7. Snapshots of air–water phase fraction in the horizontal pipe (Case 1) (continued).

(3) The depressurization at the end of cycle 1 at t = 17.2 s again causes a significant pressure gradient along the horizontal pipe, accelerating the air and water in the horizontal pipe (Figure 13). This relative rise in the air and water velocity causes the formation of new slugs. When the slug reaches the intersection (at the base of the dropshaft), the water carryover into the dropshaft due to the slug flow repeats itself as described in cycle 1 (Figures 4f and 5g,h), and the process is cycled. This entire cycle is referred to as cycle 2 in Figure 14 (t = 17.2 s to 21.35 s). It is worth mentioning that the peak water volume fraction in cycle 2 is smaller than in cycle 1 (Figure 14), indicating that the less dense mixture formed inside the dropshaft with successive cycles.

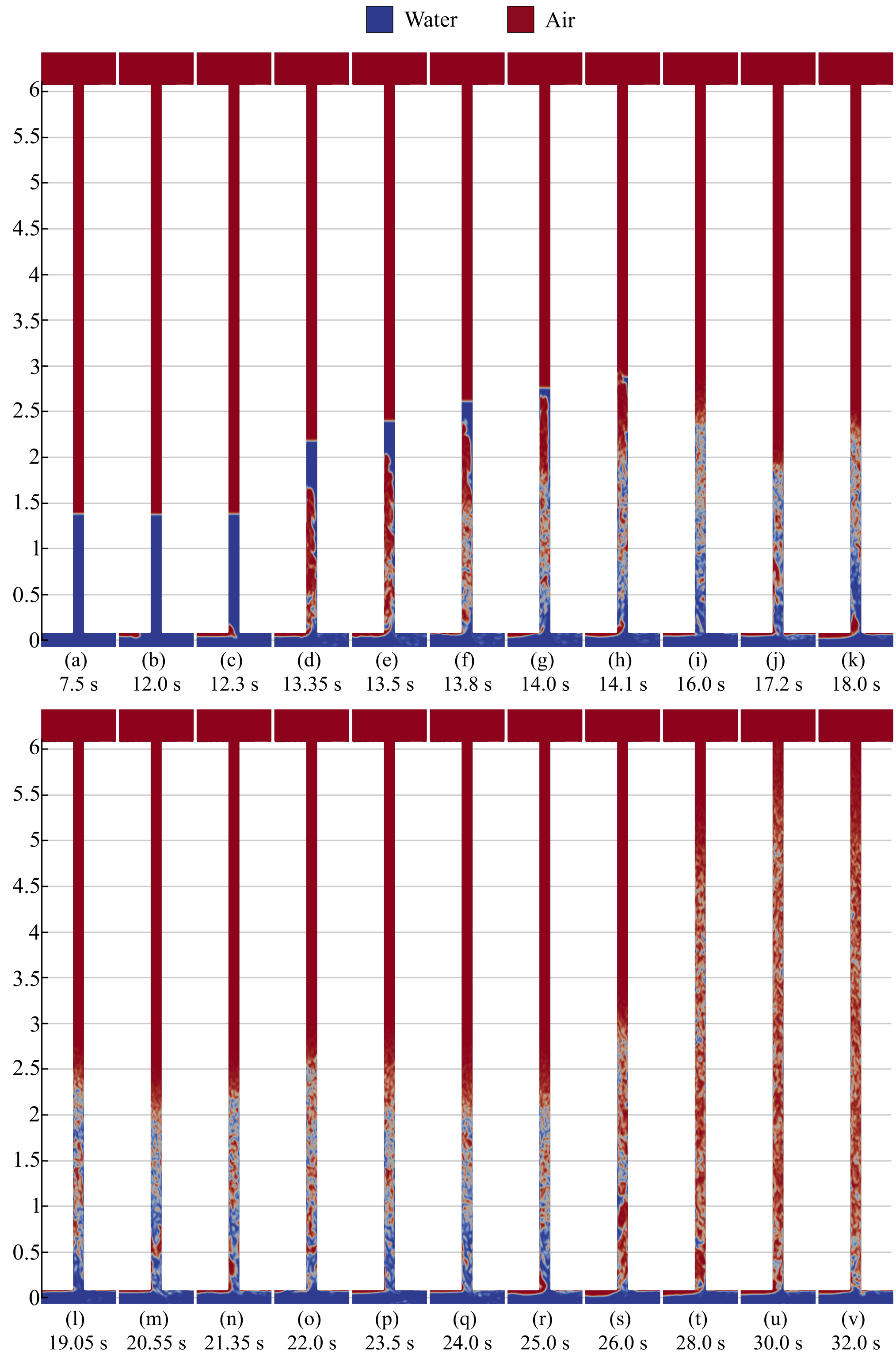

Figure 8. Snapshots of air–water phase fraction in the dropshaft (Case 1).

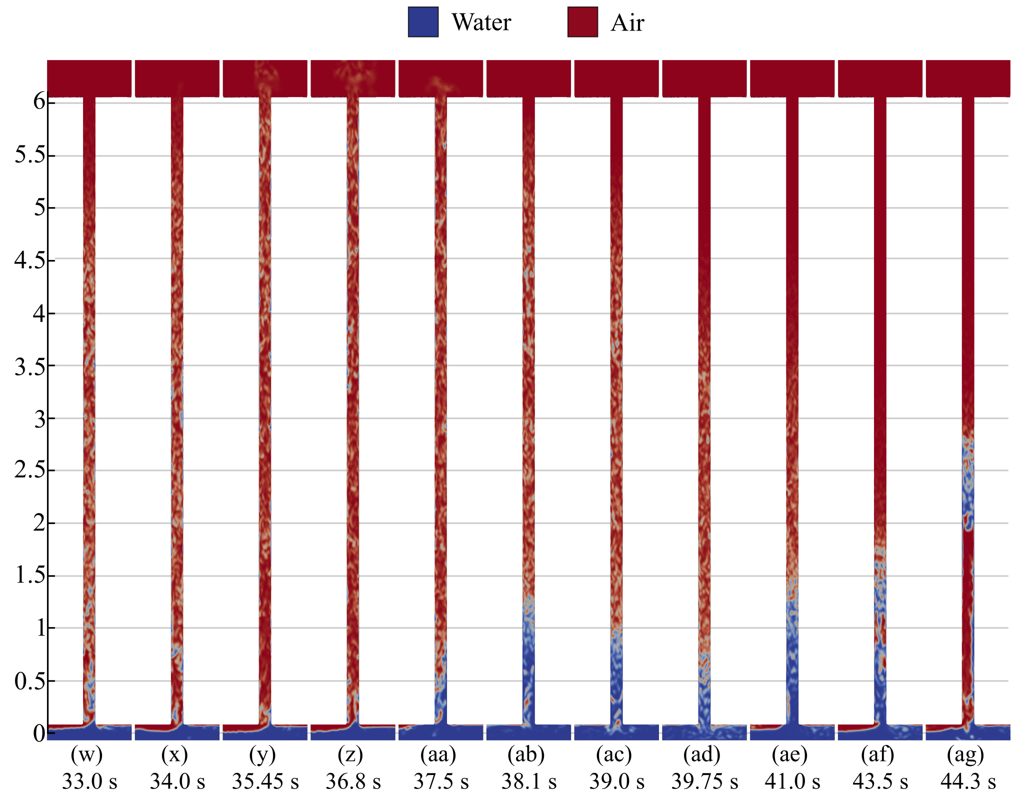

Figure 9. Snapshots of air–water phase fraction in the dropshaft (Case 1) (continued).

(4) The sequence of the rise and fall in the pressure gradient in cycle 3 is similar to that described in cycle 1 and cycle 2. The respective pressure fluctuations, the relative velocities of the air and water phases, and the water volume fraction inside the dropshaft during this cycle (t = 21.37 s to t=25.2 s) can be seen in Figures 10, 13 and 14, respectively. At this stage, the significantly less dense mixture started forming inside the dropshaft due to the continuous mixing of air due to the aforesaid cycles. At t = 35.15 s, the air–water mixture rises to the top of the dropshaft, losing water, which quickly reduces the hydrostatic pressure. The depressurization due to spillage is significantly large, accelerating the air entering the dropshaft and forming slugs inside the horizontal pipe due to KH instability (Figure 7x). At this stage, the slug is propelled violently through the dropshaft due to a significantly large pressure gradient, resulting in the eruption (Figure 9y,z). During this process, new slugs can be formed in the horizontal pipe. Once the aforementioned liquid slugs cross the junction, they are siphoned into the dropshaft, creating a partial blockage at the intersection (Figures 7y,z and 9aa,ab). The fallback of the air–water mixture can be seen in Figures 7aa,ab and 9ac,ad due to the scarcity of the air supply due to the blockage. It should be noted that the number of initial cycles required to create an initial spillage (rise of the air–water mixture to the top of the dropshaft) is dependent on the initial water level in the dropshaft and the amount of air trapped in the horizontal pipe. The discussion in this study is only limited to the first eruption; however, the study showed that subsequent eruptions are observed in the system as long as a continuous supply of water and air is provided. The detailed water holdup plots until the first eruption at sections x = 16 m, 18 m, 20 m, 22 m, and 24 m are presented in Figure 18.

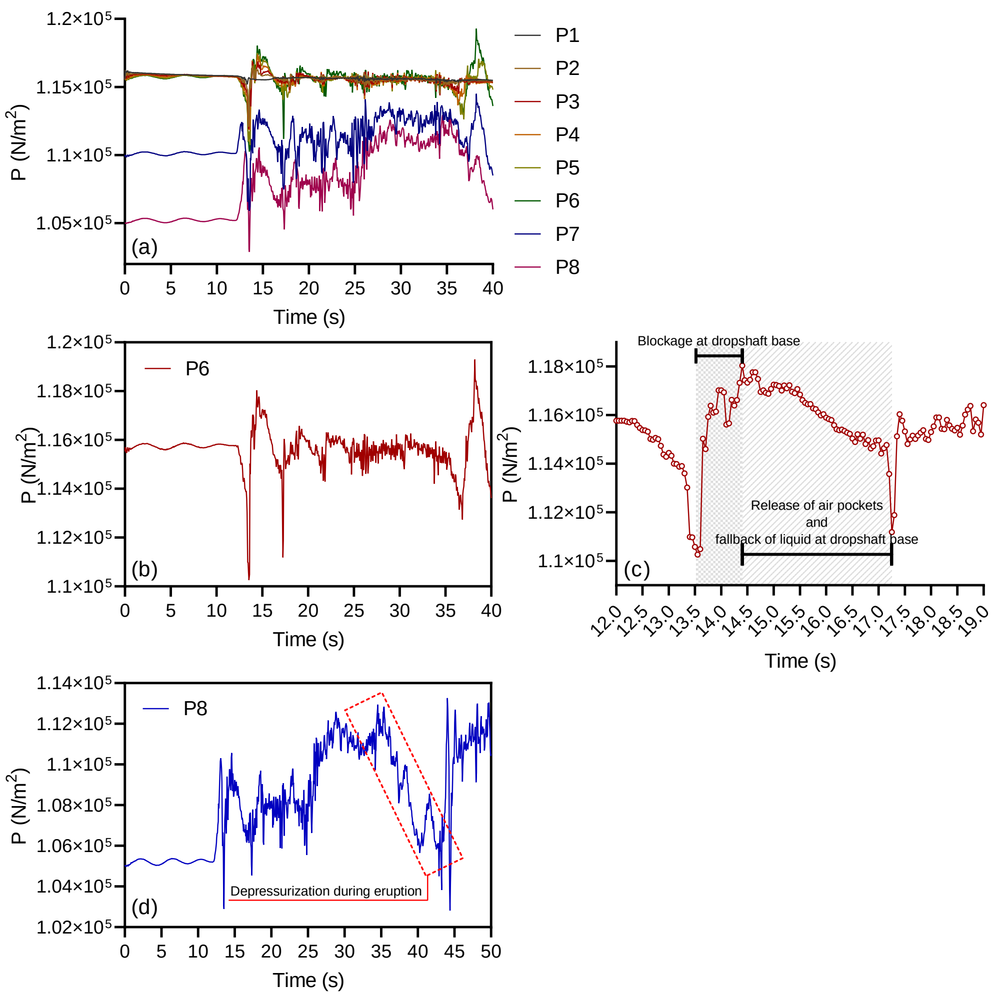

Figure 10. Results of simulation (Case 1): (**a**) pressure fluctuations recorded at key monitoring points along the horizontal pipeline and dropshaft during the geyser cycle, (**b**) P6, (**c**) zoom-in P6, and (**d**) P8.

To obtain an in-depth understanding of the flow structure inside the dropshaft and at the junction during each cycle, Figure 19 is presented. Figure 19a shows a flow structure during the blockage stage. A temporary blockage is created at the intersection due to an advancing slug, which prevents the release of the trapped air through the dropshaft. Inside the dropshaft, small bubbles in the slug cell/slug body (SB) produced a strong drag force, driving water upward, due to the large bubble–water contact area [48,49]. The film downstream of the SB also pursues the fast-moving liquid in the SB, referred to as the 'ascending film (AF)'. However, with the restricted air supply through the horizontal pipe (due to the temporary blockage at the intersection), the film decelerated its upward velocity as the shear force and buoyancy force acting on the film were not enough to balance the gravity. This flow reversal is also assisted by the directional water flow through a horizontal pipe, dragging it towards the downstream. Figure 19b describes the flow structure in the dropshaft as the next air pocket is ingested into the dropshaft after the blockage. The release of trapped air causes the SB and liquid film to move upward due to the large buoyancy and shear force caused by the airflow. With each cycle, the air–water mixture reaches higher into the dropshaft till it erupts due to the blowout of the SB and liquid film.

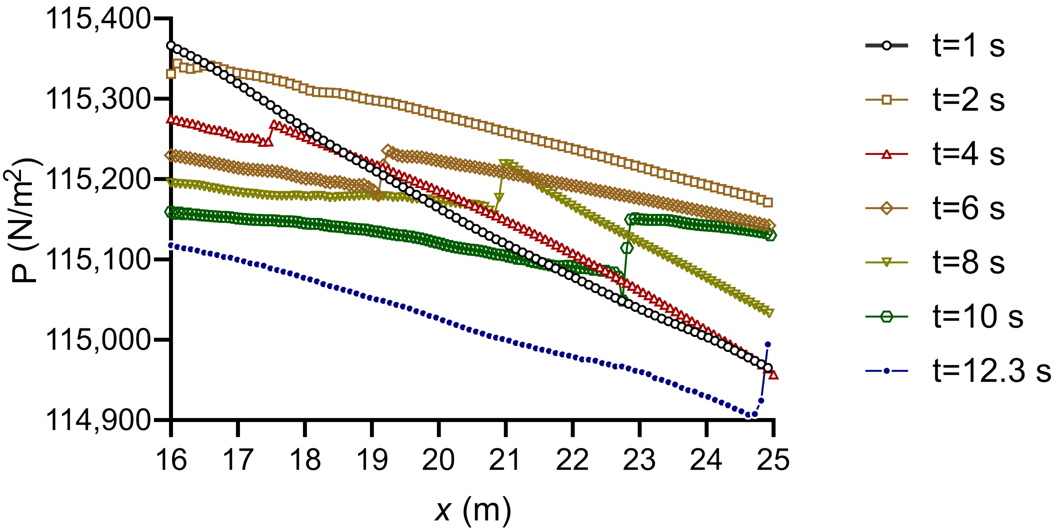

Figure 11. Pressure distribution curves of the central axis of the horizontal pipe till it reaches the bottom of the dropshaft (Case 1). The figure highlights the progressive buildup and oscillation of the pressure as air pockets travel through the horizontal pipe and interact with the dropshaft.

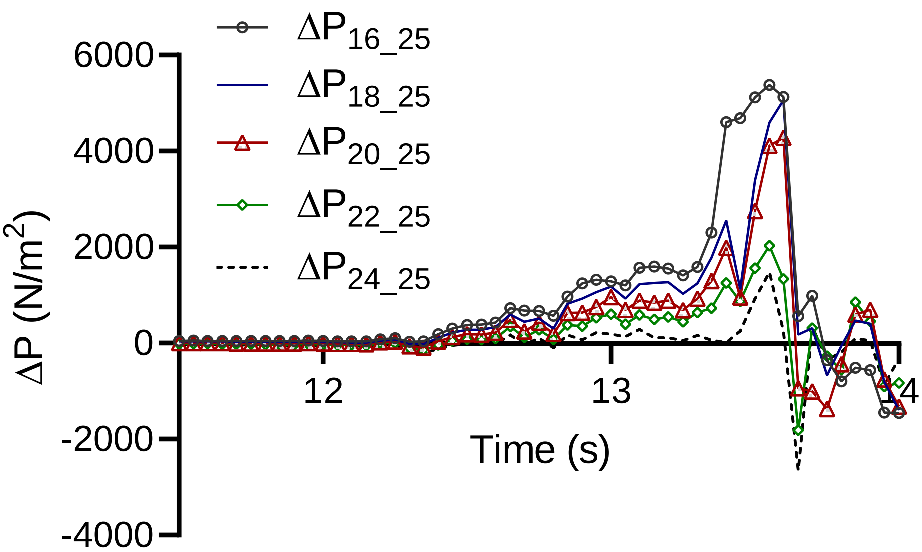

Figure 12. Differential pressure along the horizontal pipe (Case 1). The figure illustrates the pressure gradient as air pockets move through the pipe, showing regions of rapid pressure change associated with slug flow initiation.

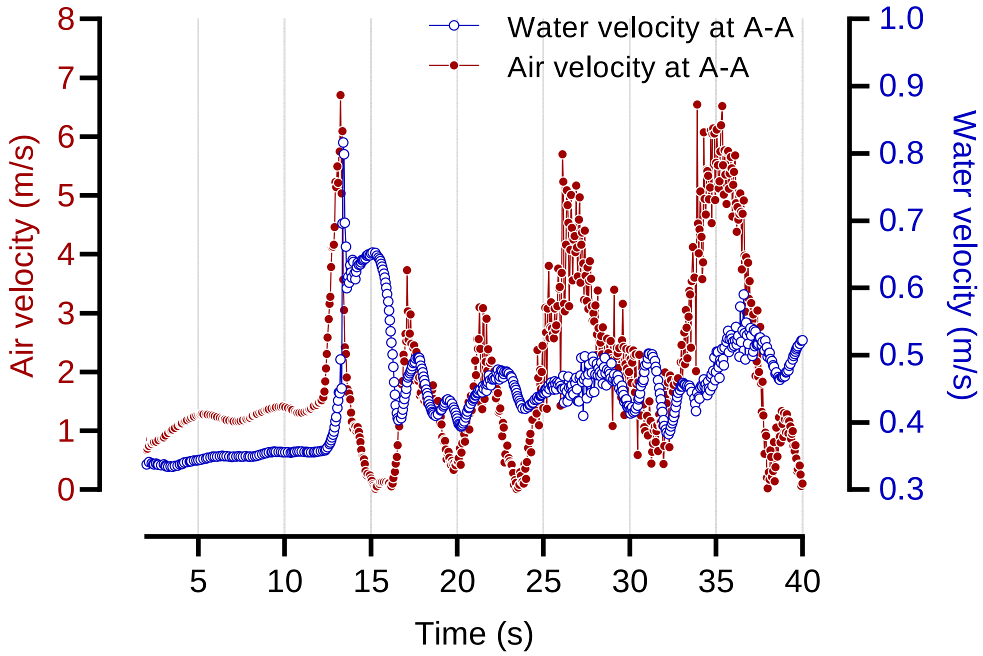

Figure 13. The velocity of water and air in the horizontal pipe at section A-A (Case 1). The figure illustrates the distinct velocity distributions of the two phases, with air accelerating more rapidly than water due to lower density and higher mobility. This velocity differential contributes to shear at the air–water interface, promoting the onset of instabilities.

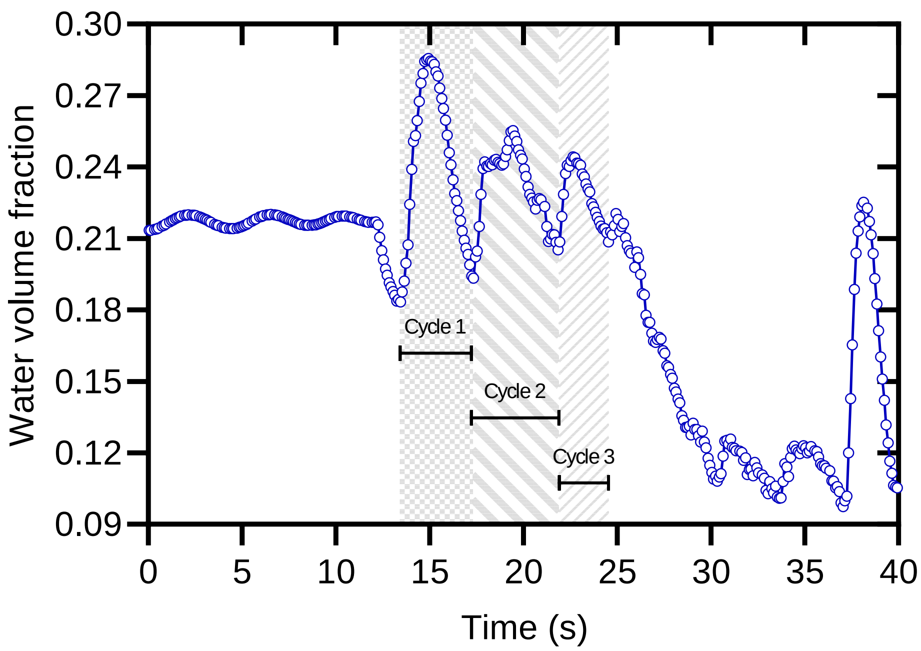

Figure 14. Temporal variation in the water volume fraction inside the dropshaft (Case 1). The figure depicts the redistribution of water during different phases of the geyser cycle, highlighting the impact of air pocket dynamics and pressure fluctuations on the water column.

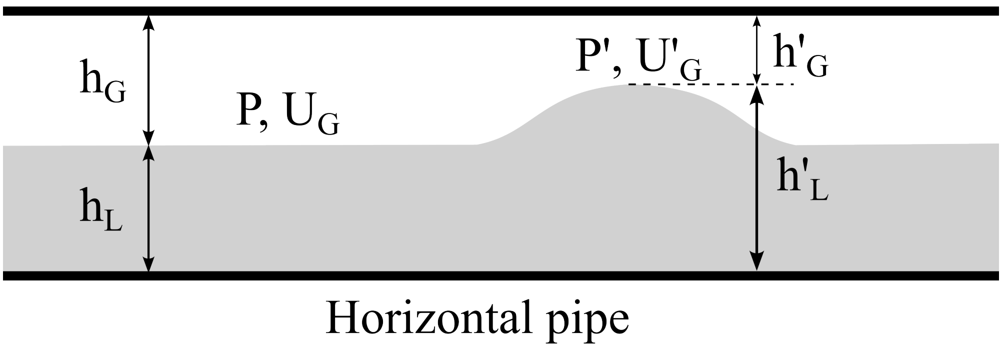

Figure 15. Schematic of interface wave instability criteria.

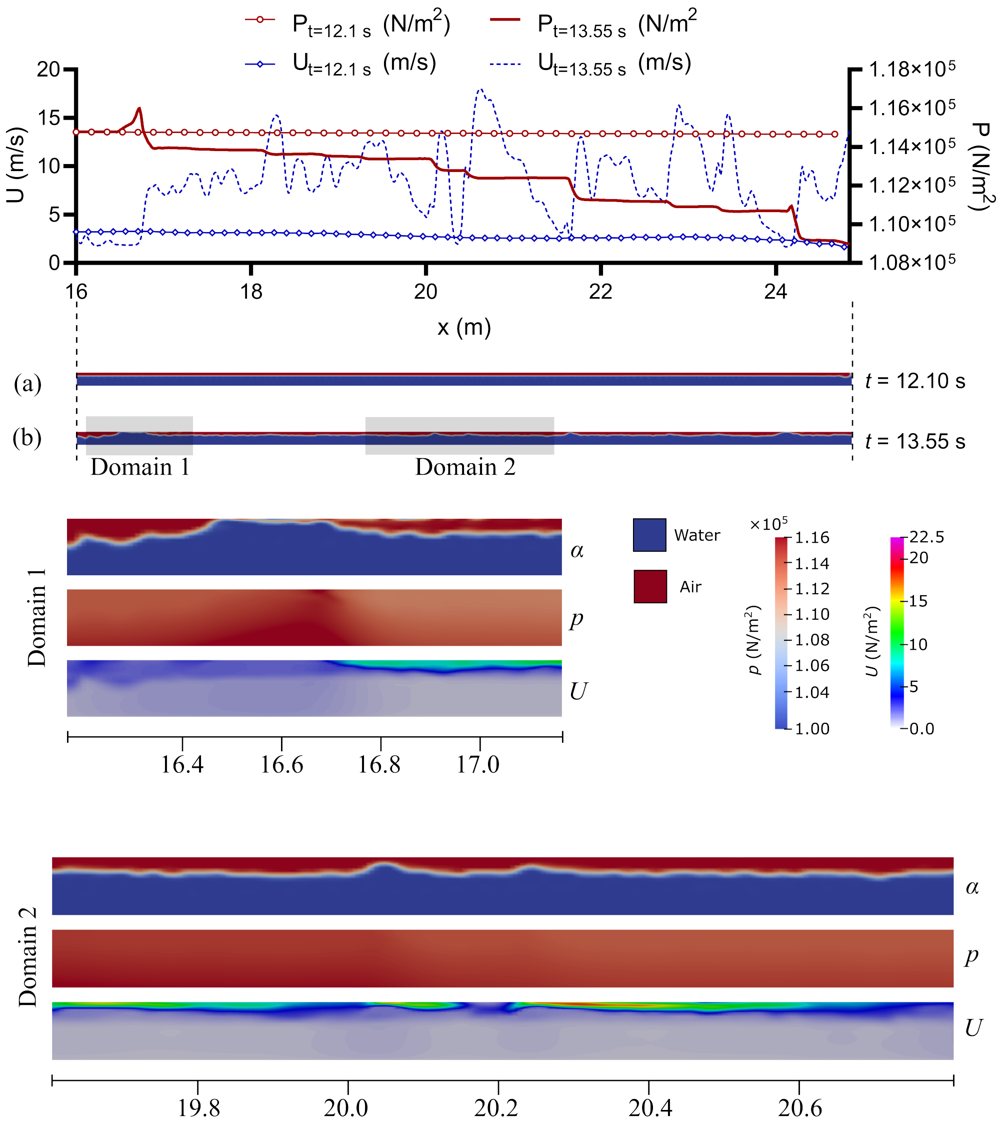

Figure 16. Aerodynamic pressure gradient and velocity variation over a wave (Case 1). The figure illustrates the interaction between the pressure gradients and velocity profiles along the wave crest and trough, highlighting how aerodynamic forces influence the wave's stability and growth. (**a**) stratified condition at t = 12.10 s, (**b**) initiation of small perturbations at t = 13.55 s.

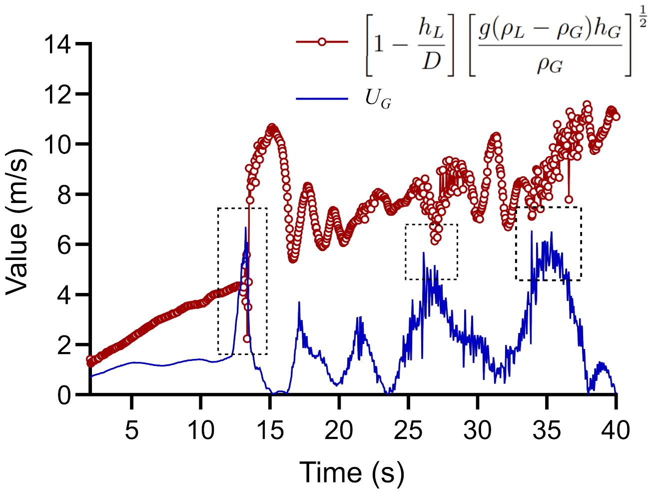

Figure 17. Plot of instability criteria (Case 1), illustrating the conditions under which flow transitions occur due to Kelvin–Helmholtz instability. The figure shows critical thresholds that trigger wave amplification and flow destabilization.

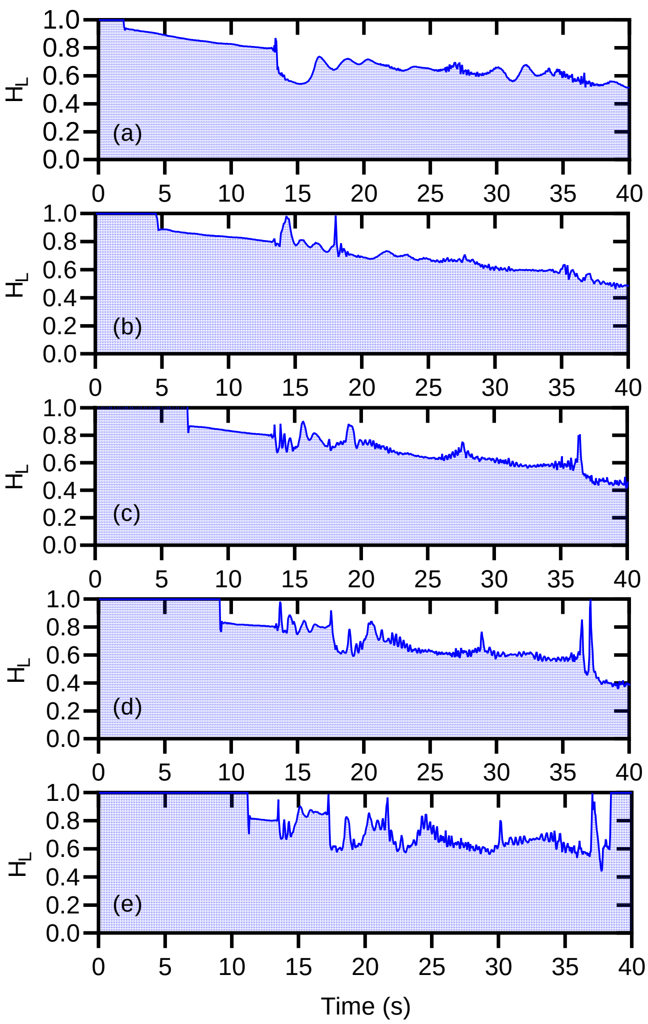

Figure 18. Water holdup at (**a**) x = 16 m, (**b**) x = 18 m, (**c**) x = 20 m, (**d**) x = 22 m, and (**e**) x = 24 m sections.

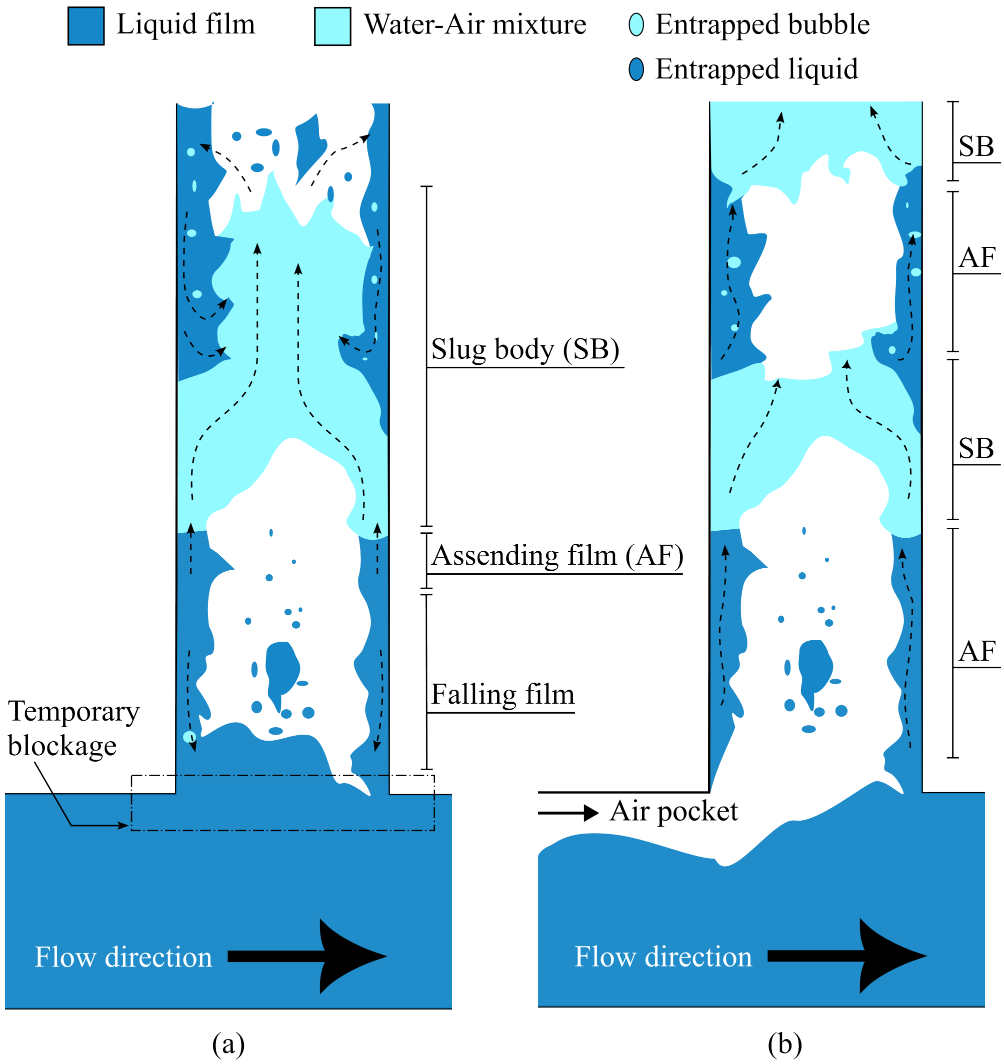

Figure 19. Visualization of flow structure within the dropshaft and at the intersection with the horizontal pipe. (**a**) during the blockage stage, (**b**) after the blockage stage.

4. Influence of Initial Water Level in Dropshaft

In this section, the effect of the initial water level in the dropshaft on the geysers is analyzed using Case 1, Case 2, and Case3.

Figures 20 and 21 show the water volume fraction in the horizontal pipe for Case 2 (i.e., $h_w/h_d = 0.5$). At t = 12.45 s, the air pocket reaches the dropshaft (Figure 20a,b). The pressures at points P6 and P8 are 133,132.5 N/m^2 and 122,565.4 N/m^2, respectively (Figures 26c and 27c). As air enters the dropshaft, the pressure at point P6 reduces to 128,208.9 N/m^2 at t = 14.2 s. The reduction at point P6 creates a significant differential pressure along the horizontal pipe, causing the water and air velocity to rise and ultimately leading to a transition from stratified to slug flow. Figure 23 shows the flow transition criteria plotted for Case 2 (Equation (13)). As shown in the plot, the velocity of air overcomes the R.H.S. of Equation (13) at t = 13.85 s to t = 14.05. The initiation of perturbations and a flow transition during this interval is corroborated by Figure 20c–e. The advancing slug and tailing mixture of rising air create a temporary blockage at the base of the dropshaft; see Figure 20f,g. The liquid film inside the dropshaft rises to 5.7 m, and, after this, it starts falling as the shear stress caused by the gas flow is not enough. The pressure drops during the fallback stage (t = 17.05 s to t = 19.05 s) at points P6 and P8 are 4419 N/m^2 and 4840.4 N/m^2, respectively. The pressure drop again creates a significant pressure gradient along the horizontal pipe, which causes the same cycle of rising and fallback of the liquid film inside the dropshaft (Figure 22f–j, at t = 19.05 s to 23.75 s). Finally, during the third cycle, the air–water mixture rises to the top of the dropshaft, causing a spillage that translates into a drastic reduction in the pressure at P6 and P8. This pressure drop creates a significant differential pressure along the horizontal pipe, accelerating the air and water, violently propelled into the dropshaft. The violent ejection of the air–water mixture can be seen in Figure 22n–s.

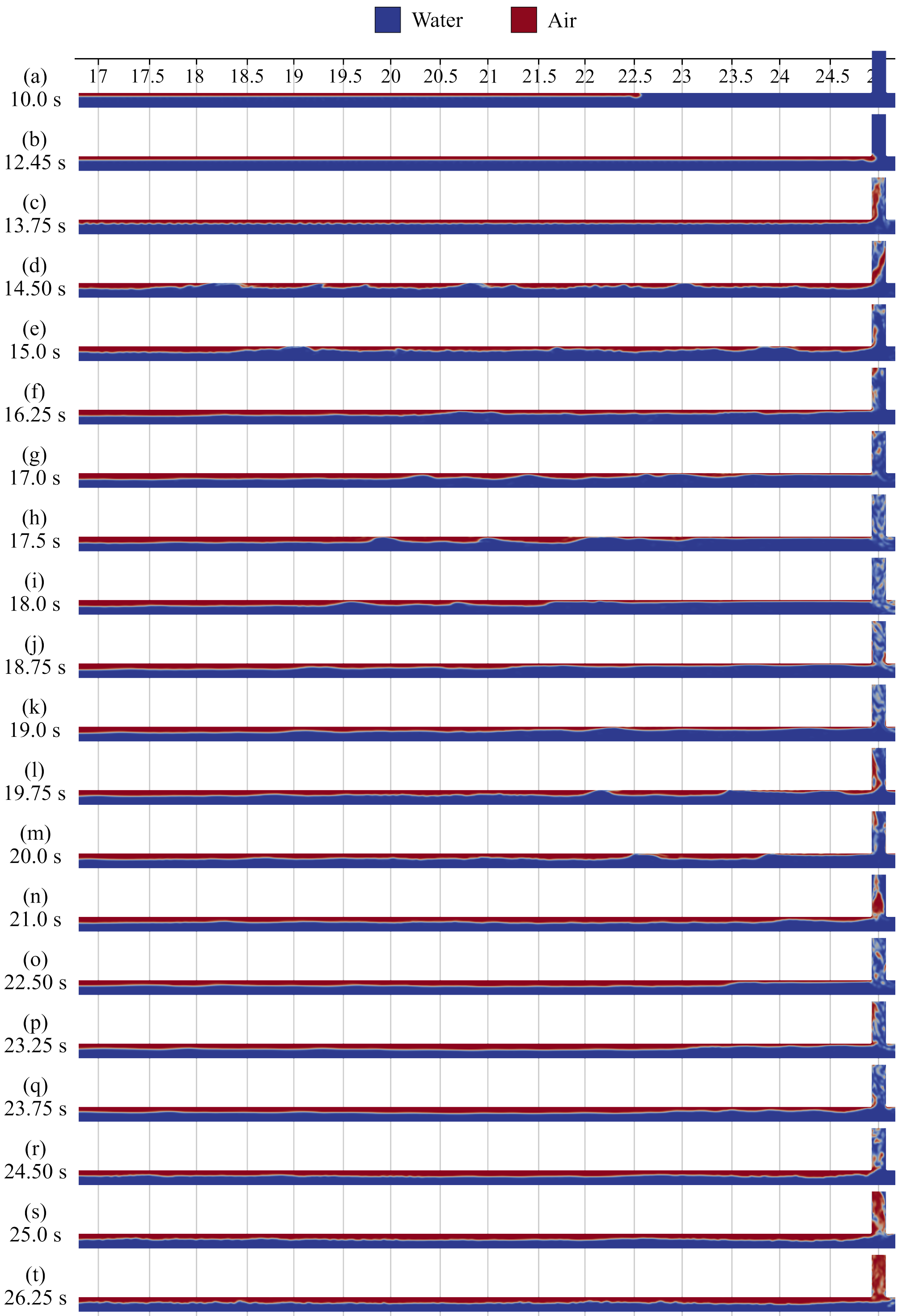

Figure 20. Snapshots of air–water phase fraction in the horizontal pipe (Case 2).

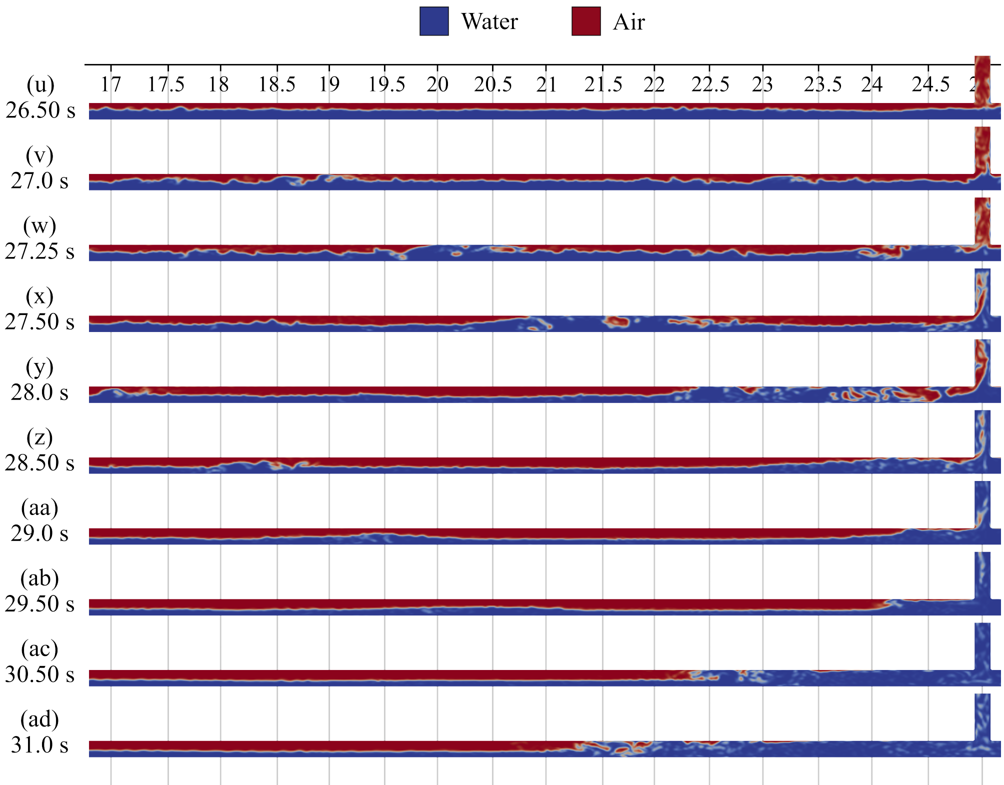

Figure 21. Snapshots of air–water phase fraction in the horizontal pipe (Case 2) (continued).

Figure 24 shows the water volume fraction in the horizontal pipe for case 3. The large air pocket approaches the dropshaft and immediately causes spillage at the top as the dropshaft is initially completely filled with water (i.e., $h_w/h_d = 1$). It can be noticed in Figures 24 and 25 that, until about 9.65 s, the large air pocket moves slowly in the horizontal pipe, without causing any noticeable variations. As more air rises through the dropshaft, it causes more water spillage. The front of the air pocket, which resembles the classical Taylor bubble rising through the dropshaft, can be seen in Figure 25b–e. This is similar to the experimental findings presented in Leon, Elayeb, and Tang (2019) [39]. The depressurization during this process is corroborated by Figures 26b and 27b from t = 10.1 s to t = 11.75 s. The rapid increase in the air–water velocities results in a flow transition due to KH instability inside the horizontal pipe from a stratified (Figure 24a,b) to wavy (Figure 24c,d) to slug flow (Figure 24e–g). Once the slugs are formed in the horizontal pipe, they are violently propelled into the dropshaft, each resulting in a violent eruption. After each sudden drop in pressure in the dropshaft (e.g., after a significant pressure gradient along a horizontal pipe), new slugs are formed and propelled into the dropshaft, creating subsequent violent eruptions. Continuous eruptions can be expected as long as the continuous supply of air and water in the system is ensured.

Figures 26 and 27 show a comparison of the pressure fluctuations at P6 and P8 for Case 1, Case 2, and Case 3. At eruption, a drastic reduction in pressure can be seen in the pressure data for all cases. The pressure variation at both points is shown using box and whisker plots (Figures 26e and 27e). It is evident that the overall pressure variation increases with an increase in the initial water level in the dropshaft. Figure 28 shows the ejection velocity at the top of the dropshaft for Case 1, Case 2, and Case 3. The maximum ejection velocities recorded for Case 1, Case 2, and Case 3 were 3.02 m/s, 5.17 m/s, and 14.58 m/s, respectively. The ejection velocity is related to the pressure gradient (between the horizontal pipe and dropshaft). The larger the pressure variation, the greater the ejection velocity. It is worth mentioning that the second or third geyser eruption has a larger intensity than the first.

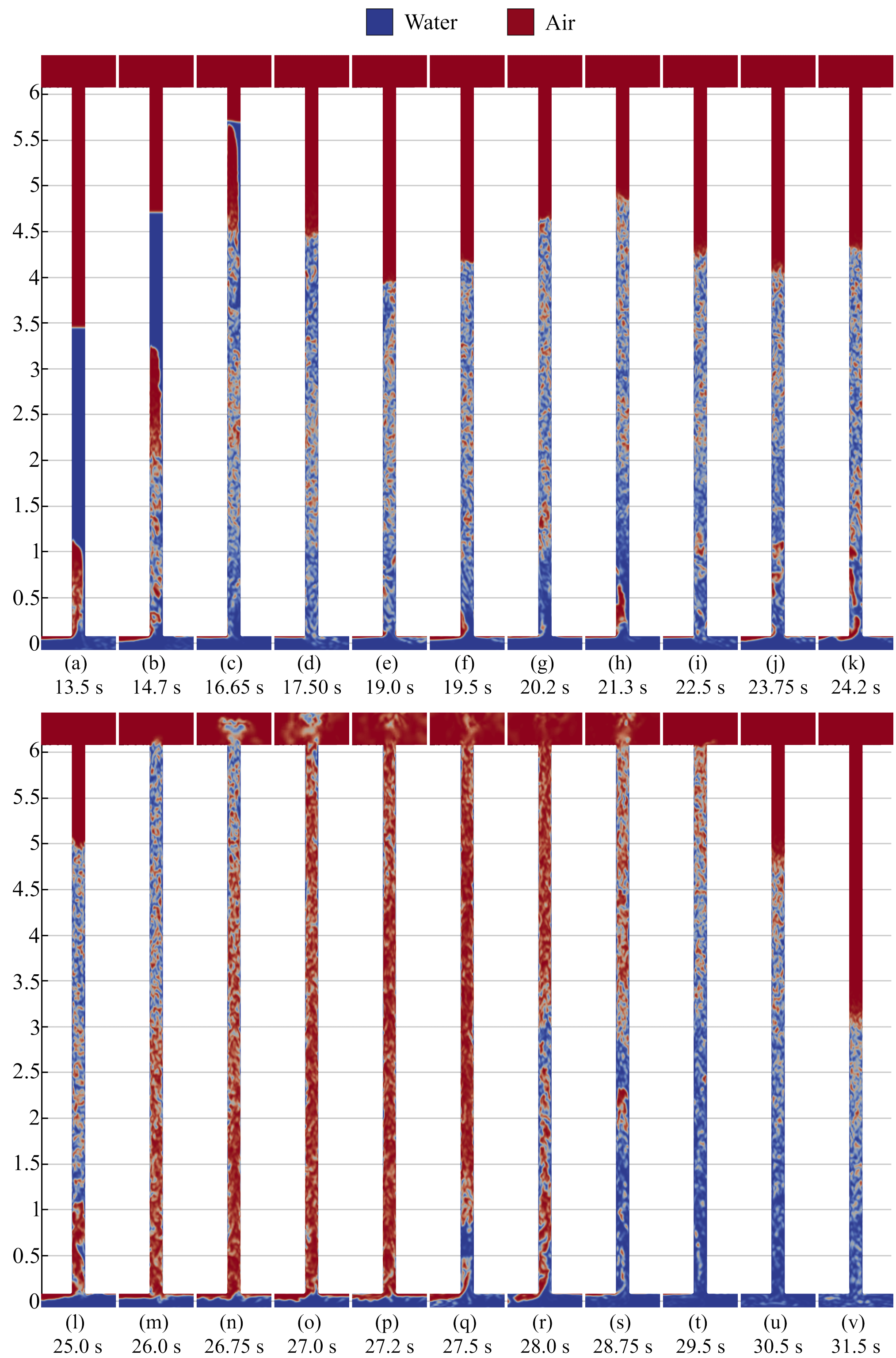

Figure 22. Snapshots of air–water phase fraction in the dropshaft (Case 2).

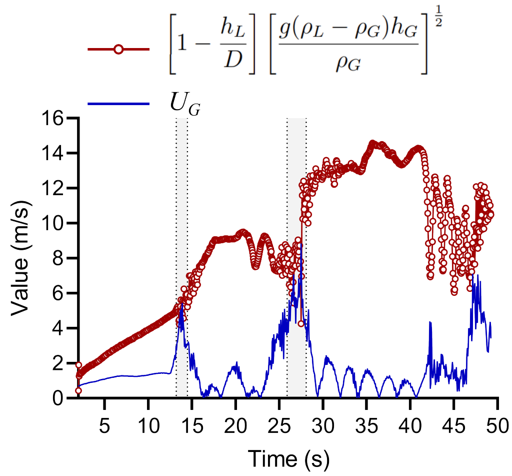

Figure 23. Plot of instability criteria (Case 2).

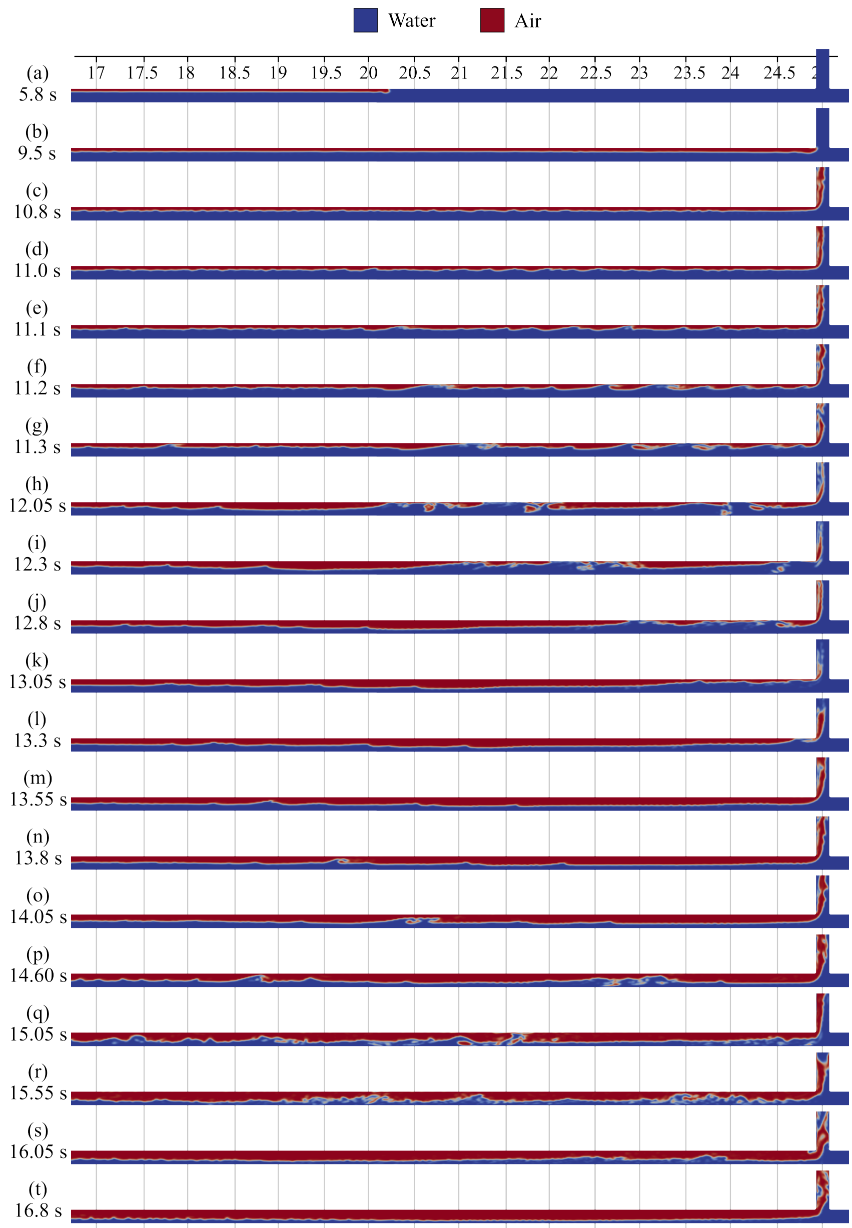

Figure 24. Snapshots of air–water phase fraction in the horizontal pipe (Case 3).

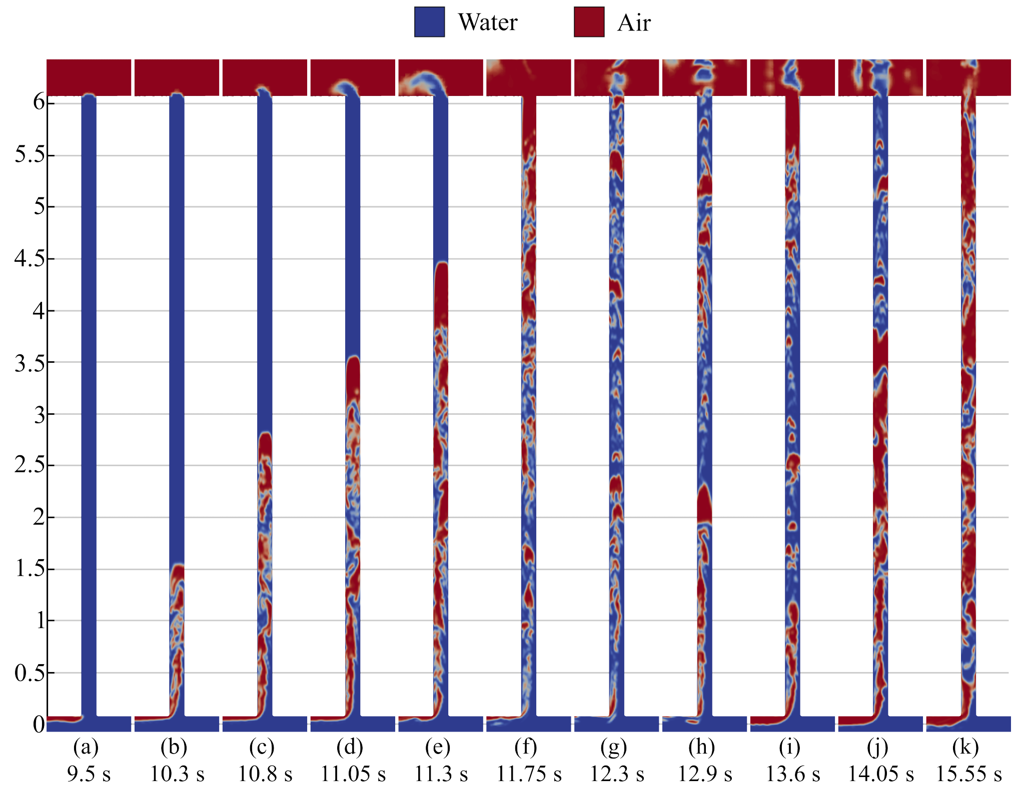

Figure 25. Snapshots of air–water phase fraction in the dropshaft (Case 3).

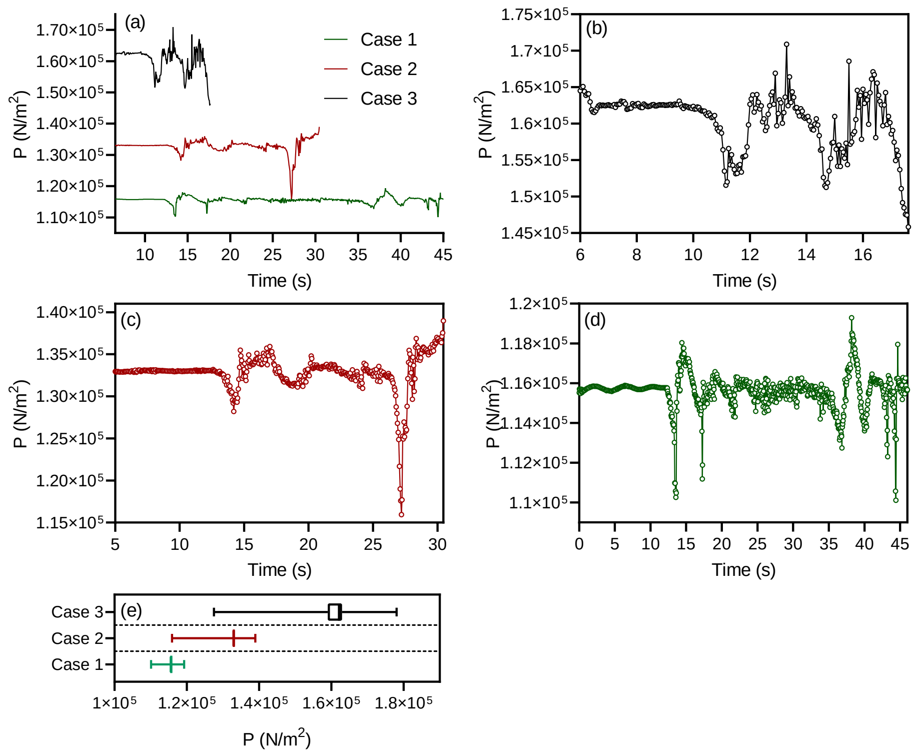

Figure 26. Results of simulation at point P6: (**a**) comparison for all three cases, (**b**) case 3, (**c**) case 2, (**d**) case 1, and (**e**) box and whisker plot presenting spread and skewness of data.

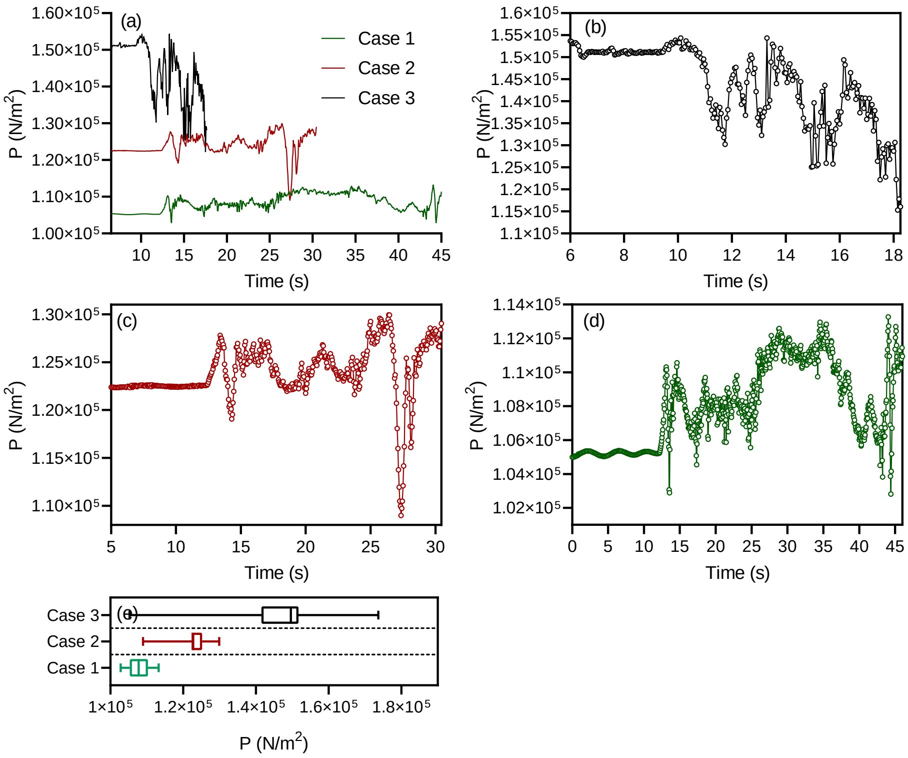

Figure 27. Results of simulation at point P8: (**a**) comparison for all three cases, (**b**) case 3, (**c**) case 2, (**d**) case 1, and (**e**) box and whisker plot presenting spread and skewness of data.

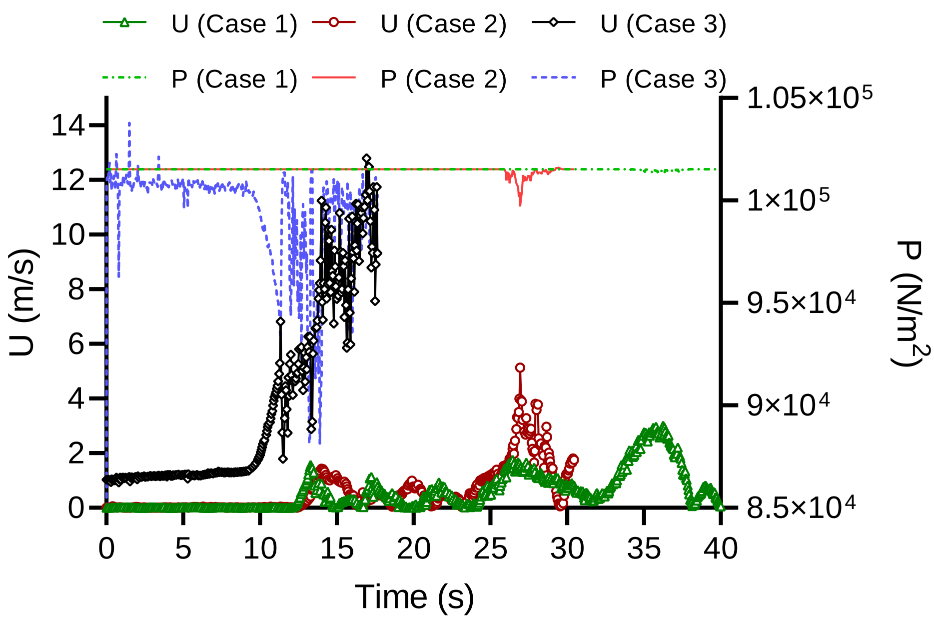

Figure 28. Velocity and pressure fluctuations at the top of the dropshaft for Case 1, Case 2, and Case 3.

5. Influence of the Ratio of the Dropshaft to Tunnel Diameter

A set of simulations was conducted in which the diameter of the dropshaft was varied (Case 2 and Case 4). The diameter of the tunnel remained constant (i.e., 0.152 m) during these simulations. These simulations aimed to determine the effect of varying the ratio between the diameter of the dropshaft to the tunnel on geyser formation. In Case 2, the diameter of the dropshaft and tunnel was 0.152 m (i.e., $D_d/D_t = 1.0$), whereas, in Case 4, the diameter of the dropshaft was 0.076 m (i.e., $D_d/D_t = 0.5$). It is found, in general, that the rise of the liquid column increases with a smaller dropshaft diameter, hence leading to earlier spillage.

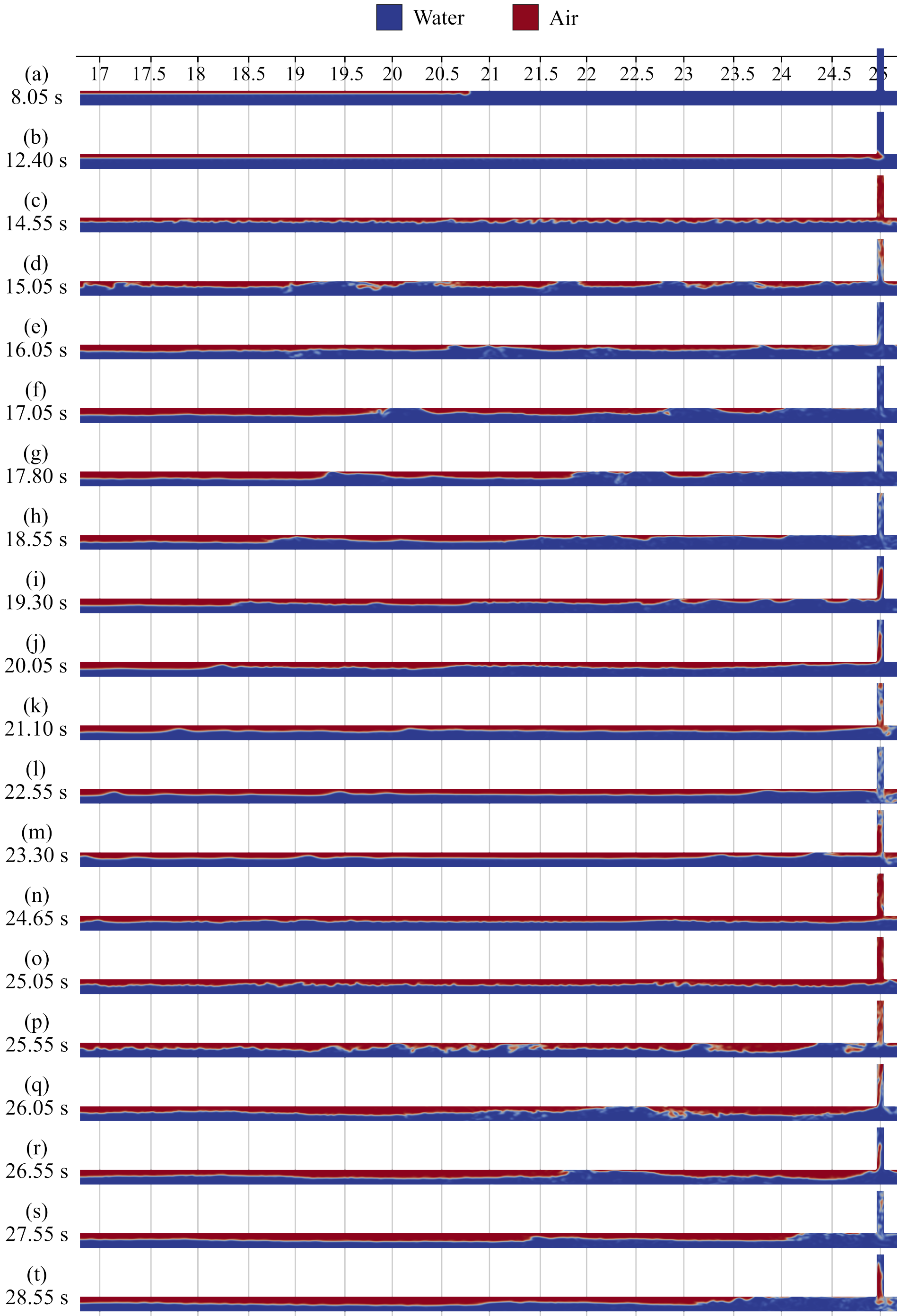

Figure 29. Snapshots of air–water phase fraction in the horizontal pipe (Case 4).

Figure 29 shows the water volume fraction in the horizontal pipe for Case 4. At t = 12.35 s, the air pocket reaches the dropshaft (Figure 29a,b). The rise of the air inside the dropshaft is shown in Figure 30a–d. With the rise of the air pocket, the pressure at P6 starts falling from 133,010.8 N/m^2 (t = 13.7 s) to 120247.1 N/m^2 (t = 14.8 s). Due to the smaller diameter of the dropshaft in Case 4, the rise of the water column increases compared to Case 2. The spillage can be noticed at t = 14.85 s in Figure 30e. A sudden drop in hydrostatic pressure due to spillage resulted in a flow transition (Figure 29c,d). Similar to Case 2, once the slugs are formed in the horizontal pipe (due to a sudden drop in hydrostatic pressure), they are propelled into the dropshaft, creating a temporary blockage at the base of the dropshaft. The rise of the propelled slug into the dropshaft is higher, causing the overall pressure variation to be larger compared to Case 2 (Figure 32b). The system goes through multiple cycles of rise and fall in the liquid and again erupts at t = 24.55 s (Figure 30u) and t = 26.55 s (Figure 31aa). In Figure 32c, we illustrate the eruption velocity at the top of the dropshaft. The maximum velocity in eruption in Case 4 is 9.41 m/s at t = 25.15 s (i.e., 116% higher than the maximum eruption velocity in Case 2). It is noteworthy that the second eruption was higher in intensity than the first eruption.

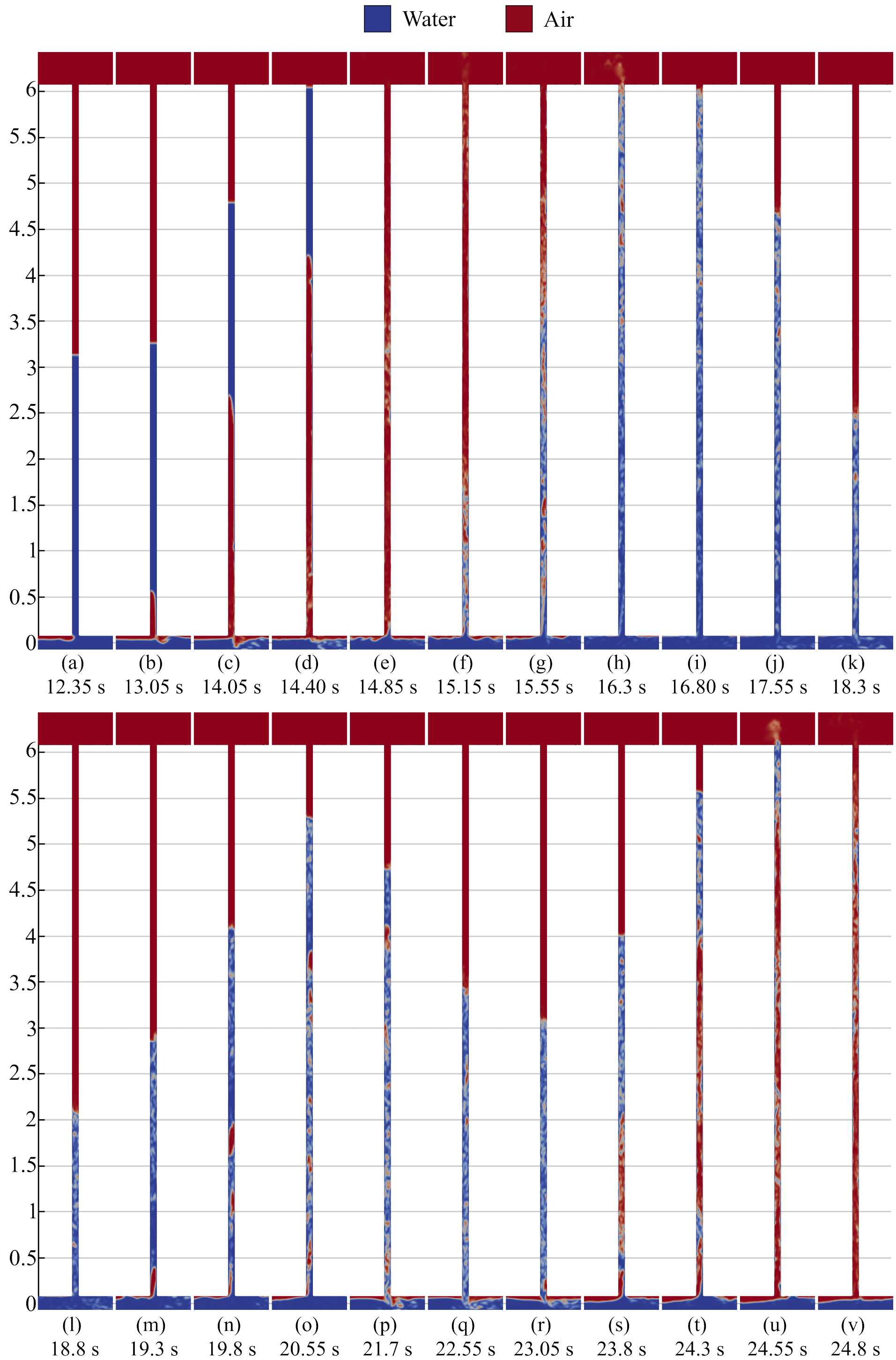

Figure 30. Snapshots of air–water phase fraction in the dropshaft (Case 4).

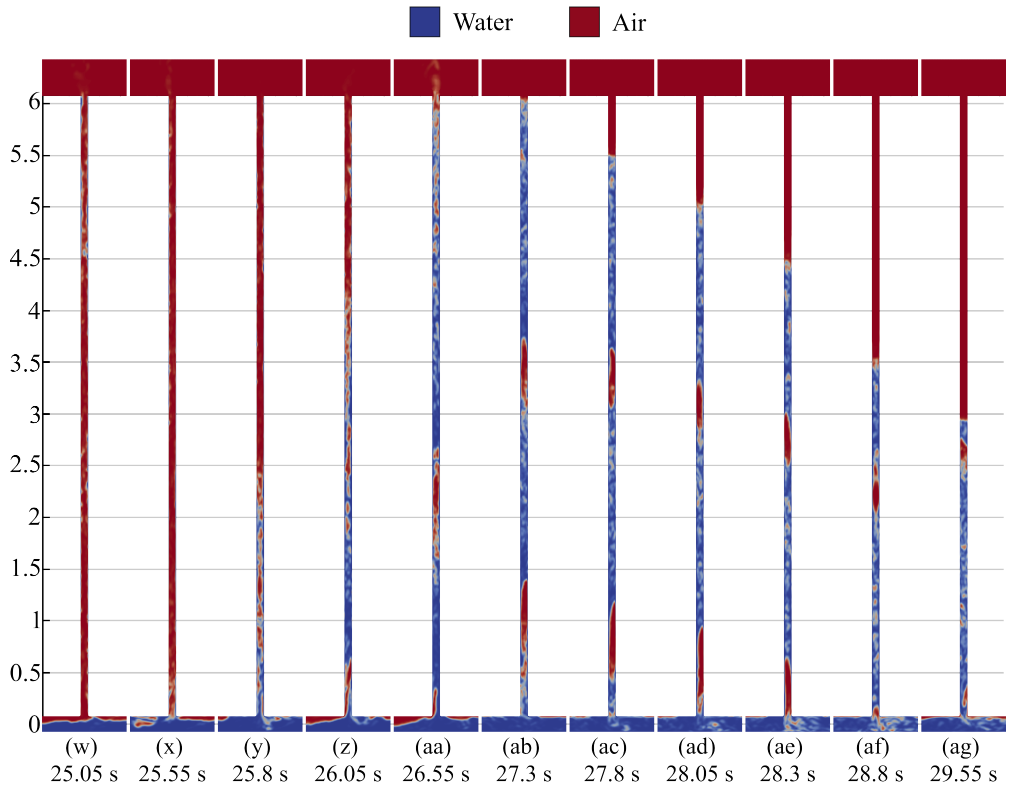

Figure 31. Snapshots of air–water phase fraction in the dropshaft (Case 4) (continued).

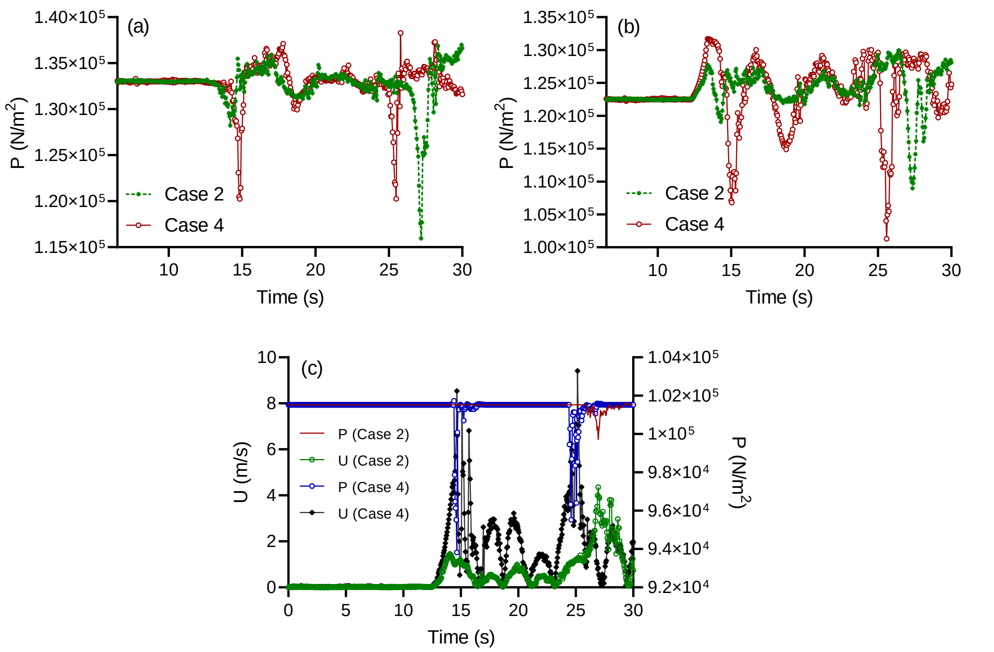

Figure 32. Results of simulation for Case 2 and Case 4: (**a**) P6, (**b**) P8, and (**c**) velocity and pressure fluctuations at the exit of the dropshaft.

Numerical accuracy is a crucial component of every numerical simulation. This was ensured in the current work by using sufficiently fine meshes to yield grid-independent solutions. Failure to accomplish this would prevent instabilities from escalating. The influence of the tunnel diameter was not analyzed in this study. As per the experimental study by Lin and Hanratty (1987) [50], a large velocity is needed in a large pipe for a flow transition from stratified to slug. However, it also has an indirect, conceivably less significant effect on the other flow patterns because the stabilizing effect of gravity in small-diameter pipes is weaker. The slug region is large in a small horizontal pipe, and the large-amplitude waves (concerning the pipe diameter) are created more readily.

This study offers helpful recommendations to enhance stormwater management systems by identifying the key mechanism responsible for geyser eruption. The numerical analysis illustrates the effects of the initial water depth and dropshaft shape on geyser development and intensity. The performance and resilience of stormwater systems under extreme flow conditions can be improved by directly incorporating these results into their design. For example, it has been demonstrated that the accumulation of greater pressure gradients at lower dropshaft diameters increases the intensity of eruptions. According to this finding, greater dropshaft diameters might be used in crucial locations to improve energy dissipation and lessen the intensity of air–water interactions. Likewise, the amplification of the geyser intensity with greater initial water depths highlights how crucial it is to control the upstream flow conditions in order to avoid building up too much pressure.

6. Conclusions

This paper describes the detailed mechanisms that lead to violent geysers in storm-sewer and combined sewer systems using 3D numerical modeling, with a particular focus on partially filled dropshaft conditions. The effect of the initial water in the dropshaft and the dropshaft diameter on geyser formation were analyzed using four cases. It should be noted that, regardless of these specific factors, all geyser events share the same fundamental characteristics. The key results are as follows.

(1) The mechanism of geyser formation in this study is not just limited to the dropshaft being initially in the completely filled state (i.e., $h_w/h_d = 1$, which may not represent field conditions), as discussed in Leon (2019) [5], but it provides a detailed explanation of the role of a smaller initial water depth on geyser formation (i.e., $h_w/h_d = 0.23$ and 0.5). By focusing on the partially filled state, this study not only addresses a wider range of field-relevant scenarios but also provides a comprehensive explanation of geyser phenomena that encompasses both partially and fully filled conditions.

(2) A low initial water depth in the dropshaft does not ensure immediate spillage at the top of the dropshaft. The cycle of rise and fallback in the liquid film inside the dropshaft creates a less dense mixture, causing the subsequent rise of the air–water mixture and ultimately giving rise to spillage. The eruption is evident by the drastic reduction in the hydrostatic head at the intersection, creating a significantly large pressure gradient along the horizontal pipe, resulting in a flow transition.

(3) The intensity of geyser eruption (ejection velocity) increases with the increase in the initial water level in the dropshaft. This is because the overall pressure gradient variation along the horizontal pipe is more significant, resulting in the violent propulsion of the air in the dropshaft. For Case 3 ($h_w/h_d = 1$), the maximum eruption velocity reached 14.58 m/s; such a high velocity could be responsible for the violent eruptions observed in the field.

(4) The effect of the riser diameter was studied using numerical models (Case 2 and Case 4). It is found that the strength of the geyser eruption increased with a smaller dropshaft diameter. This can be used as a base study in designing geyser mitigation techniques in which the eruption intensity can be reduced by proposing a section of the dropshaft to be relatively larger than the horizontal pipe.

The applicability of this research ranges from the aspect of practical engineering to that of theoretical domains. Thus, for stormwater systems, the provided insights into the dropshaft geometry and pressure dynamics offer scientific grounds for the retrofitting of the existing infrastructure with new technologies, such as integrating air venting systems, enlarging sections of dropshafts, or optimizing pipe inclinations to dissipate pressure gradients. Additionally, the research informs design standards for new infrastructure, enhancing the resilience to urban flooding and improving public safety. Apart from stormwater management systems, the methods and outcomes are relevant to similar two-phase flow scenarios occurring in combined sewer systems, industrial pipelines, and energy systems. This study provides a framework to simulate and analyze geyser behavior, thus providing tools to address challenges in regions with different topographies, different rainfall intensities, and different designs of drainage systems. Future efforts should also explore incorporating environmental variables, such as sediment interactions, temperature gradients, and transient inflows, which will broaden the model's scope and applicability, ensuring its utility across diverse operational scenarios.

Author Contributions: Conceptualization, S.R.Z.; methodology, S.R.Z.; software, S.R.Z.; validation, S.R.Z., P.M., A.S., A.S.L., V.P. and Y.Y.I.; formal analysis, S.R.Z.; investigation, A.S.L.; resources, A.S.L., V.P. and Y.Y.I.; data curation, S.R.Z.; writing—original draft preparation, S.R.Z.; writing—review and editing, S.R.Z., P.M., A.S., A.S.L., V.P. and Y.Y.I.; visualization, S.R.Z.; supervision, A.S.L.; project administration, A.S.L.; funding acquisition, A.S.L. All authors have read and agreed to the published version of the manuscript.

Funding: This research was funded by the National Science Foundation (NSF) grant number 1928850.

Data Availability Statement: The data presented in this study are available on request from the corresponding author.

Acknowledgments: The authors gratefully acknowledge the financial support of the National Science Foundation (NSF) under grant number 1928850 and the financial support of a Florida International University Graduate School Dissertation Year Fellowship (DYF). The authors would also like to acknowledge the contributions of the late Cheng-Xian Lin.

Conflicts of Interest: The authors declare no conflict of interest.

Nomenclature

∇	gradient function (m^{-1})
α	water volume fraction (-)
κ	curvature of the interface (-)
μ	kinematic viscosity (m^2/s)
ρ_a	density of air (kg/m^3)
ρ_w	density of water (kg/m^3)
ρ	phase mixture density (kg/m^3)
μ_a	kinetic viscosity of air (m^2/s)
μ_w	kinetic viscosity of water (m^2/s)
h_w	water level in the dropshaft (m)
h_a	height of atmosphere domain (m)
h_d	height of the dropshaft (m)
L_{u_1}	length of upstream pipe from the extreme upstream end to air tank (m)
L_{u_2}	length of upstream pipe from air tank to dropshaft (m)
L_d	length of downstream pipe (m)
D_t	diameter of horizontal pipe (m)
D_d	diameter of dropshaft (m)
$c_{v,a}$	specific heat capacity of air at constant volume (J/kg K)
$c_{v,w}$	specific heat capacity of water at constant volume (J/kg K)
T	temperature field (K)
t	time (s)
$\boldsymbol{U}$	velocity field (m/s)
k	turbulence kinetic energy (m^2/s^2)
ε	turbulence dissipation rate (m^2/s^3)
$\boldsymbol{g}$	acceleration due to gravity (m/s^2)

$\boldsymbol{U_c}$	compression velocity (m/s)
P	pressure field (N/m^2)
μ_{eff}	thermal eddy diffusivity (kg/m s)
σ	surface tension (N/m)
R	universal gas constant (J/kg K)
$\boldsymbol{x}$	position vector (m)

References

1. Granata, F. Dropshaft cascades in urban drainage systems. *Water Sci. Technol.* **2016**, *73*, 2052–2059. [CrossRef] [PubMed]
2. Shen, J.; Wu, J.; Ma, F. Hydraulic characteristics of stepped spillway dropshafts. *Sci. China Technol. Sci.* **2019**, *62*, 868–874. [CrossRef]
3. Guo, Q.; Song, C.C.S. Surging in Urban Storm Drainage Systems. *J. Hydraul. Eng.* **1990**, *116*, 1523–1537. [CrossRef]
4. Wright, S.J.; Lewis, J.W.; Vasconcelos, J.G. Geysering in Rapidly Filling Storm-Water Tunnels. *J. Hydraul. Eng.* **2011**, *137*, 112–115. [CrossRef]
5. Leon, A.S. Mechanisms that lead to violent geysers in vertical shafts. *J. Hydraul. Res.* **2019**, *57*, 295–306. [CrossRef]
6. Qian, Y.; Zhu, D.Z.; Liu, L.; Shao, W.; Edwini-Bonsu, S.; Zhou, F. Numerical and Experimental Study on Mitigation of Storm Geysers in Edmonton, Alberta, Canada. *J. Hydraul. Eng.* **2020**, *146*, 04019069. [CrossRef]
7. Li, J.; McCorquodale, A. Modeling the Transition from Gravity to Pressurized Flows in Sewers. In Proceedings of the Urban Drainage Modeling, Orlando, FL, USA, 20–24 May 2001; pp. 134–145. [CrossRef]
8. Hamam, M.A.; McCorquodale, J.A. Transient conditions in the transition from gravity to surcharged sewer flow. *Can. J. Civ. Eng.* **1982**, *9*, 189–196. [CrossRef]
9. Zhou, F.; Hicks, F.E.; Steffler, P.M. Transient Flow in a Rapidly Filling Horizontal Pipe Containing Trapped Air. *J. Hydraul. Eng.* **2002**, *128*, 625–634. [CrossRef]
10. Zhou, F.; Hicks, F.E.; Steffler, P.M. Observations of air-water interaction in a rapidly filling horizontal pipe. *J. Hydraul. Eng.* **2002**, *128*, 635–639. [CrossRef]
11. Wright, S.J.; Lewis, J.W.; Vasconcelos, J.G. Physical Processes Resulting in Geysers in Rapidly Filling Storm-Water Tunnels. *J. Irrig. Drain. Eng.* **2011**, *137*, 199–202. [CrossRef]
12. Pozos-Estrada, O.; Pothof, I.; Fuentes-Mariles, O.A.; Dominguez-Mora, R.; Pedrozo-Acuña, A.; Meli, R.; Peña, F. Failure of a drainage tunnel caused by an entrapped air pocket. *Urban Water J.* **2015**, *12*, 446–454. [CrossRef]
13. Wright, S.J. A new look at geyser formation in sewer systems. *J. Water Manag. Model.* **2021**, *29*, 1–18. [CrossRef]
14. Mahyawansi, P.; Zanje, S.R.; Sharifi, A.; McDaniel, D.; Leon, A.S. Experimental and numerical investigation of a small scale storm sewer geyser. *J. Hydraul. Res.* **2024**, *62*, 25–38. [CrossRef]
15. Mahyawansi, P.; Zanje, S.R.; Sharifi, A.; McDaniel, D.; Leon, A.S. Experimental investigation of storm sewer geyser using a large-scale setup. *Phys. Fluids* **2024**, *36*, 052101. [CrossRef]
16. Miller, S.T.; Jasak, H.; Boger, D.A.; Paterson, E.G.; Nedungadi, A. A pressure-based, compressible, two-phase flow finite volume method for underwater explosions. *Comput. Fluids* **2013**, *87*, 132–143. [CrossRef]
17. Jasak, H. Error Analysis and Estimation for the Finite Volume Method with Applications to Fluid Flows. 1996. Available online: https://www.croris.hr/crosbi/publikacija/ocjenski-rad/445133 (accessed on 19 January 2022).
18. Ferrer, P.M.; Causon, D.M.; Qian, L.; Mingham, C.G.; Ma, Z.H. A multi-region coupling scheme for compressible and incompressible flow solvers for two-phase flow in a numerical wave tank. *Comput. Fluids* **2016**, *125*, 116–129. [CrossRef]
19. Greenshields, C. OpenFOAM v6 User Guide. 2018. Available online: https://doc.cfd.direct/openfoam/user-guide-v6/index (accessed on 21 January 2022).
20. Cerbe, G.; Wilhelms, G. Basics of Thermodynamics. In *Proceedings of the Technical Thermodynamics*; Carl Hanser: Munich, Germany, 2021; pp. 17–51. [CrossRef]
21. Weller, H.G. *Derivation, Modelling and Solution of the Conditionally Averaged Two-Phase Flow Equations*; Technical Report TR/HGW/02; Nabla Ltd.: Pune, India, 2002.
22. Rusche, H. Computational Fluid Dynamics of Dispersed Two-Phase Flows at High Phase Fractions. Ph.D. Thesis, University of London, London, UK, 2003.
23. Tryggvason, G.; Bunner, B.; Esmaeeli, A.; Juric, D.; Al-Rawahi, N.; Tauber, W.; Han, J.; Nas, S.; Jan, Y.J. A Front-Tracking Method for the Computations of Multiphase Flow. *J. Comput. Phys.* **2001**, *169*, 708–759. [CrossRef]
24. Koch, M.; Lechner, C.; Reuter, F.; Köhler, K.; Mettin, R.; Lauterborn, W. Numerical modeling of laser generated cavitation bubbles with the finite volume and volume of fluid method, using OpenFOAM. *Comput. Fluids* **2016**, *126*, 71–90. [CrossRef]
25. Chegini, T.; Leon, A.S. Numerical investigation of field-scale geysers in a vertical shaft. *J. Hydraul. Res.* **2019**, *1686*, 1–13. [CrossRef]

26. Zanje, S.R.; Mahyawansi, P.; Leon, A.S.; Lin, C.X. CFD Modeling of Storm Sewer Geysers in Partially Filled Dropshafts. In Proceedings of the World Environmental and Water Resources Congress 2022, Atlanta, Georgia, 5–8 June 2022; pp. 1187–1195. [CrossRef]
27. Shih, T.H.; Liou, W.W.; Shabbir, A.; Yang, Z.; Zhu, J. A new k-ε eddy viscosity model for high reynolds number turbulent flows. *Comput. Fluids* **1995**, *24*, 227–238. [CrossRef]
28. OpenCFD. Mesh Generation with the snappyHexMesh Utility. Available online: https://www.openfoam.com/documentation/user-guide/4-mesh-generation-and-conversion/4.4-mesh-generation-with-the-snappyhexmesh-utility (accessed on 2 November 2022).
29. Zanje, S.R.; Bian, L.; Verma, V.; Yin, Z.; Leon, A.S. Siphon Break Phenomena Associated with Pipe Leakage Location. *J. Fluids Eng.* **2022**, *144*, 111202. [CrossRef]
30. CFD_Online. CFD Online—Turbulence Properties, Conversions & Boundary Estimations. Available online: https://www.cfd-online.com/Tools/turbulence.php (accessed on 2 November 2022).
31. OpenCFD. OpenFOAM: User Guide: k-Epsilon. Available online: https://www.openfoam.com/documentation/guides/latest/doc/guide-turbulence-ras-realizable-k-epsilon.html (accessed on 2 November 2022).
32. Chegini, T.; Leon, A.S. Comparison of Various Turbulence Models for Violent Geysers in Vertical Pipes. In Proceedings of the World Environmental and Water Resources Congress 2018, Minneapolis, MN, USA, 3–7 June 2018; pp. 99–108. [CrossRef]
33. Courant, R.; Friedrichs, K.; Lewy, H. On the partial difference equations of mathematical physics. *IBM J. Res. Dev.* **1967**, *11*, 215–234. [CrossRef]
34. Lee, D.; Park, H.; Ha, T.; Shin, S.; Cox, D.T. Numerical modeling of hydrodynamics on an elevated residential structure from varied wave and surge conditions using OpenFOAM. *Coast. Eng.* **2022**, *178*, 104204. [CrossRef]
35. Issa, R.I. Solution of the implicitly discretised fluid flow equations by operator-splitting. *J. Comput. Phys.* **1986**, *62*, 40–65. [CrossRef]
36. Ferziger, J.H.; Perić, M.; Street, R.L. *Computational Methods for Fluid Dynamics*; Springer: Berlin/Heidelberg, Germany, 2002; Volume 3.
37. Bhusare, V.H.; Dhiman, M.K.; Kalaga, D.V.; Roy, S.; Joshi, J.B. CFD simulations of a bubble column with and without internals by using OpenFOAM. *Chem. Eng. J.* **2017**, *317*, 157–174. [CrossRef]
38. Leer, B.V. Towards the ultimate conservative difference scheme. *J. Comput. Phys.* **1997**, *135*, 229–248. [CrossRef]
39. Leon, A.S.; Elayeb, I.S.; Tang, Y. An experimental study on violent geysers in vertical pipes. *J. Hydraul. Res.* **2019**, *57*, 283–294. [CrossRef]
40. Liu, Y.; Li, W.Z. Numerical simulation on two-phase bubbly flow split in a branching T-junction. *Int. J. Air-Cond. Refrig.* **2011**, *19*, 253–262. [CrossRef]
41. Taitel, Y.; Dukler, A.E. A model for predicting flow regime transitions in horizontal and near horizontal gas-liquid flow. *AIChE J.* **1976**, *22*, 47–55. [CrossRef]
42. Kordyban, E. Horizontal Slug Flow: A Comparison of Existing Theories. *J. Fluids Eng.* **1990**, *112*, 74–83. [CrossRef]
43. Johnston, A.J. Transition from stratified to slug regime in countercurrent flow. *Int. J. Multiph. Flow* **1985**, *11*, 31–41. [CrossRef]
44. Wu, X.; Wang, Z.; Dong, M.; Ge, Q.; Dong, L. Simulation Study on the Development Process and Phase Interface Structure of Gas-Liquid Slug Flow in a Horizontal Pipe. *Front. Energy Res.* **2021**, *9*, 762471. [CrossRef]
45. Saini, S.; Banerjee, J. Physics of aeration in slug: Flow visualization analysis in horizontal pipes. *J. Vis.* **2021**, *24*, 917–930. [CrossRef]
46. Sanchis, A.; Johnson, G.W.; Jensen, A. The formation of hydrodynamic slugs by the interaction of waves in gas-liquid two-phase pipe flow. *Int. J. Multiph. Flow* **2011**, *37*, 358–368. [CrossRef]
47. Pao, W.; Memon, Z.Q. Numerical evaluation of separation efficiency in converging T-junction with slug flow. *Int. J. Numer. Methods Heat Fluid Flow* **2019**, *30*, 3515–3534. [CrossRef]
48. Delfos, R.; Rops, C.; Kockx, J.; Nieuwstadt, F. Measurement of the recoalescence flux into the rear of a Taylor bubble. *Phys. Fluids* **2001**, *13*, 1141–1150. [CrossRef]
49. Wang, Z.; Deng, Y.; Pan, Y.; Jin, Y.; Huang, F. Experimentally investigating the flow characteristics of airlift pumps operating in gas-liquid-solid flow. *Exp. Therm. Fluid Sci.* **2020**, *112*, 109988. [CrossRef]
50. Lin, P.Y.; Hanratty, T.J. Effect of pipe diameter on flow patterns for air-water flow in horizontal pipes. *Int. J. Multiph. Flow* **1987**, *13*, 549–563. [CrossRef]